RESEARCH ARTICLE

Smart Selective Antennas System (SSAS): Improving 4G LTE Connectivity for UAVs Using Directive Selective Antennas

EMANUELE PAGLIARI[1], **LUCA DAVOLI**[1], (Member, IEEE),
GIORDANO CICIONI[2], (Graduate Student Member, IEEE),
VALENTINA PALAZZI[2], (Senior Member, IEEE), **PAOLO MEZZANOTTE**[2], (Member, IEEE),
FEDERICO ALIMENTI[2], (Senior Member, IEEE), **LUCA ROSELLI**[2], (Fellow, IEEE), AND
GIANLUIGI FERRARI[1], (Senior Member, IEEE)

[1]Department of Engineering and Architecture, University of Parma, 43124 Parma, Italy
[2]Department of Engineering, University of Perugia, 06123 Perugia, Italy

Corresponding author: Emanuele Pagliari (emanuele.pagliari@unipr.it)

ABSTRACT In this paper, the prototypical deployment of a Multiple-Input-Multiple-Output (MIMO) antennas system, denoted as Smart Selective Antennas System (SSAS), aiming at mitigating inter-cell interference effects of cellular networks for in-flight Unmanned Aerial Vehicles (UAVs), is discussed. In detail, the proposed SSAS is beneficial to increase the communication reliability over existing cellular networks, especially with regard to complex Beyond Visual Line of Sight (BVLOS) drones' missions and applications. Its deployment is motivated as existing 4G Long Term Evolution (LTE) cellular networks (as well as 5G networks) are mainly designed and optimized for terrestrial utilization, thus not taking into account interference effects on flying connected devices. The prototypical implementation of the SSAS has been expedient to conduct multiple experimental flights with a drone at different altitudes, collecting performance results and validating the proposed SSAS as a viable solution for inter-cell interference mitigation.

INDEX TERMS Antennas, cellular networks, connectivity, drones, UAV, LTE.

I. INTRODUCTION

The use of Unmanned Aerial Vehicles (UAVs, often known as drones) for a wide plethora of heterogeneous applications has grown exponentially (and is expected to increase even more) in the last (and next) decade [1], when thousands of drones are expected to fly above (heterogeneously connected) *smart cities* to provide different kinds of services, ranging from surveillance tasks, (industrial) building inspections, up to the delivery of goods or first aid missions [2].

The associate editor coordinating the review of this manuscript and approving it for publication was Davide Ramaccia.

Various (often commercial) solutions can already perform autonomous flights over wide areas of several square kilometers [3]. However, on the technical side, there are still several challenging limits to overcome, especially when dealing with Beyond Visual Line of Sight (BVLOS) flight missions, in which communication must be supported, without direct visibility, between the *in-flight* UAV and the pilot or control center on the ground. In detail, such a flight mission could rely on a direct *point-to-point* wireless communication between the parties only in the case of limited range missions, where the communication interface's radio signal is sufficiently strong to provide a good link quality

suitable for both Command & Control (C2) and video/data stream for pilot or mission center.

In general, commercially available drones may exploit different wireless communication protocols, with entry level UAV solutions relying on the use of Wi-Fi-based protocols (working in 2.4 GHz and 5.8 GHz ISM unlicensed frequency bands) and, thus, providing a bi-directional communication channel sufficiently reliable to allow the pilot to flight in obstacle-free environments for several hundreds of meters. Alternatively, advanced commercial UAVs can use proprietary communication protocols (still operating in 2.4 GHz and 5.8 GHz bands): an example is given by the OcuSync [4] protocol, designed and deployed by DJI and able to guarantee operational ranges of: several kilometers in direct visibility conditions and a few hundreds of meters in BVLOS scenarios. Finally, there exist enterprise products [5] already exploiting 4G LTE cellular networks (especially as a backup link for BVLOS missions) to transfer collected data (mainly videos or images) from UAV to cloud and, then, from cloud to control center.

Terrestrial cellular networks are the best logical candidate for enhanced BVLOS UAV applications, given their widespread diffusion and reliable architecture connecting billions of devices across the world. However, despite the wide diffusion and limited cost of the 4G LTE network adapters, together with their small footprint (making them easily integrable into aerial platforms), their use on UAVs is still limited (as highlighted in the literature) mainly as a backup solution for non essential data, especially because of inter-cell interference issues. More in detail, existing 4G LTE and 5G cellular networks can provide low latency and high data rate communication links, but they have been designed, deployed, and optimized for terrestrial utilization, since most of the connected terminals (e.g., smartphones, cars, SIM-based devices, etc.) are generally located and moving on the ground or in the first tens of meters of altitude. On the technical side, this means that networks topologies, Base Transceiver Station (BTS)-mounted antennas, and frequency re-use schemes—a general pictorial representation is shown in Figure 1—between nearby cells, have been optimized to minimize (or completely avoid) the inter-cell interference on ground-connected terminals.

In European countries, commercial UAVs can typically fly at an altitude between 50 m and 120 m Above Ground Level (AGL) according to the European Union Aviation Safety Agency (EASA) regulations [6]. However, upon permission, it is possible to fly at higher altitudes, depending on the specific application which drones are involved in. Therefore, a UAV-mounted cellular modem might have a direct visibility with multiple BTSs of different cells, thus experiencing a strong inter-cell interference since the system can receive signals also from nearby cells using the same frequencies, in the end corrupting the communication and making it unreliable on both the cell border and in a wide area around the cell itself. The negative effects of inter-cell interference have been experimentally revealed through radio
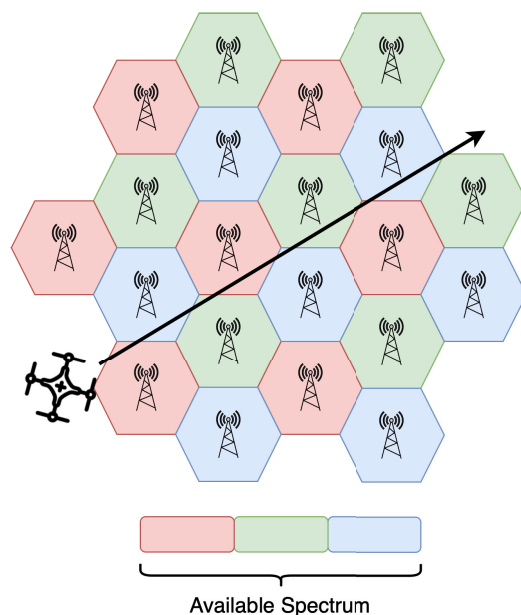

FIGURE 1. Typical frequency re-use plan for a standard cellular network.

signal quality measurements carried out during several test flights at different altitudes in the neighborhood of the city of Sabbioneta, Italy, and have also been confirmed by literature works discussed in Section III. Unfortunately, this interference problem may be stronger in all those environments where a large number of small cells is present: for instance, this happens in urban contexts, where a massive amount of pico- and femto-cells can be present in a very limited area, then leading to an intensive frequency reuse.

In this paper, we investigate the adoption of cellular connectivity for UAV applications, proposing innovative solutions to overcome the inter-cell interference problem. Then, we detail the architecture and the deployment of a prototypical system, denoted as Smart Selective Antennas System (SSAS), carrying out an experimental performance analysis in an open field in northern Italy and proposing viable improvements. In detail, we aim to foster the deployment of BVLOS applications to improve the network capabilities of these UAVs relying on existing terrestrial 4G LTE cellular networks. From an economic perspective (in terms of development costs), the proposed SASS is quite attractive: the most challenging aspect is related to the deployment of (much) smaller and lightweight directional antennas. Therefore, this system can be seen as a temporary solution useful towards the deployment of 5G and even 6G cellular networks, which may natively take into account aerial connectivity problems faced by 4G cellular networks.

The main contributions of this work can be summarized as follows.

- We evaluate the in-flight 4G LTE radio quality indexes with omni-directional antennas to underline the inter-cell interference problem.
- We investigate the inter-cell interference topic and possible strategies to minimize it.

- We present the architecture and a prototypical deployment of the SSAS, relying on both Commercial-Off-The-Shelf (COTS) and custom components.
- We design two possible SSAS antenna selection algorithms.
- We define a reliable and repeatable experimental methodology, suitable to verify the SSAS performance with both the proposed selection algorithms and with respect to commercial omni-directional antennas.
- We use the gathered data to evaluate relevant performance metrics and parameters.
- We compare the collected data to evaluate the performance, according to the defined performance metrics, as a function of the setup.
- We clearly identify weaknesses and strengths of the SSAS on the basis of the obtained experimental results.
- We propose relevant future research topics and possible improvements for the SSAS.

The remainder of this paper is organized as follows. Section II presents the preliminary data collected during several experimental flights, with the aim to investigate the adoption of 4G cellular connectivity on a UAV adopting traditional omni-directional antennas. In Section III, a literature overview on UAV-oriented cellular communications is presented, analyzing their advantages and disadvantages. In Section IV, we present our proposed SSAS solution, detailing its architecture and technical reasons. Section V illustrates the testing environment used to validate the SSAS' performance, while an experimental performance analysis is carried out in Section VI. Finally, improvements regarding the SSAS and future research directions are discussed in Section VII, while final remarks are given in Section VIII.

II. IN-FLIGHT MEASUREMENT WITH TRADITIONAL OMNI-DIRECTIONAL ANTENNAS

Before investigating the existing literature, as anticipated in Section I, the inter-cell interference (together with its negative effects) has been experimentally analyzed through radio signal quality measurements obtained thanks to various experimental flights in northern Italy—in the neighborhood of the city of Sabbioneta, Italy—at different altitudes. The behaviour of the main 4G LTE radio signal quality indexes, namely the Signal-to-Interference-plus-Noise Ratio (SINR), the Reference Signal Received Quality (RSRQ), and the Reference Signals Received Power (RSRP) have been investigated.

- According to [7], in 4G LTE networks, the Received Signal Strength Indicator (RSSI) (dimension: [mW]) is a parameter providing information related to the received wide band power (measured in all the symbols within the measurement bandwidth), including thermal noise as well as the noise generated in the receiver. Therefore, the RSSI measures the average power of the signal received by the cellular modem and includes the power from the connected BTS signal, as well as other interfering signals, such as the ones arriving from nearby cells. The

RSSI can thus be defined

$$\text{RSSI} = S_{\text{tot}} + I_{\text{tot}} + N_{\text{tot}} \tag{1}$$

where: S_{tot} (dimension: [mW]) is the useful received signal power of the connected cell measured over all the 12 Resource Elements (RE) subcarriers defined by the 4G standard [7], while I_{tot} (dimension: [mW]) and N_{tot} (dimension: [mW]) are instead the cumulative interference and thermal noise over the 12 REs subcarriers, respectively.

- The RSRP (dimension: [mW]) is another key parameter useful to verify the 4G LTE connectivity quality. According to [7], it indicates the received useful signal power level, incoming from the connected BTS, averaged over all the used LTE REs within the designated measurement frequency bandwidth. The RSRP can be computed as

$$\text{RSRP} = \frac{1}{N_{\text{RE}}} \sum_{i=1}^{N_{\text{RE}}} P_{r,i} \tag{2}$$

where: N_{RE} is the number of usable REs within the measurement frequency bandwidth; and $P_{r,i}$ (dimension: [mW]) is the power contribution of the i-th RE, $i \in \{1, \ldots, N_{\text{RE}}\}$;

- The RSRQ (adimensional) takes into account both the strength of the reference signals of the connected BTS as well as the level of noise and interference components. It is used to assess the overall quality of the received signals, thus allowing the modem to decide which cell to connect with. According to [7], it can be derived from the RSSI and RSRP as

$$\text{RSRQ} = \frac{N_{\text{PRB}} \cdot \text{RSRP}}{\text{RSSI}} \tag{3}$$

where: N_{PRB} is the number of Physical Resource Blocks (PRBs);

- The SINR (adimensional) measures the ratio of the useful signal's power to the combined power of interference and background noise, thus quantifying how well the desired signal stands out from unwanted signals and noise. It is used by the modem to calculate the Channel Quality Indicator (CQI) and, therefore, has a direct impact on the throughput of the communication link. The SINR is defined as

$$\text{SINR} = \frac{S_{\text{tot}}}{I_{\text{tot}} + N_{\text{tot}}} \tag{4}$$

where: S_{tot}, I_{tot} and N_{tot} are detailed in Eq. (1). Since S_{tot} depends on the number of used subcarriers of the measurement bandwidth, it is possible to express it as

$$S_{\text{tot}} = \frac{N_{\text{RE}}}{N_{\text{PRB}_{\text{used}}}} \cdot 12 \cdot N_{\text{PRB}} \cdot RSRP \tag{5}$$

where $N_{\text{RE}}/N_{\text{PRB}_{\text{used}}}$ indicates the percentage of used subcarriers and it is equal to 1 when all the subcarriers
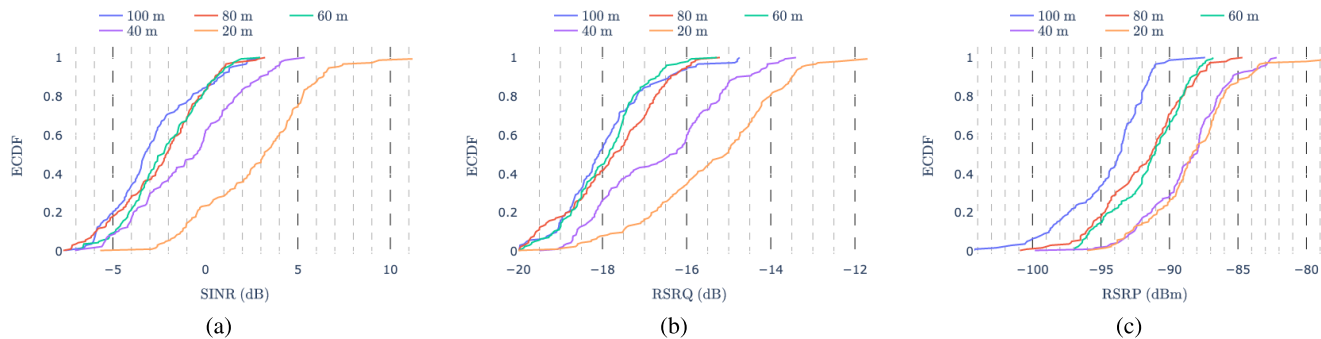
FIGURE 2. Omni-directional antennas ECDF at different altitudes of: (a) SINR, (b) RSRQ and (c) RSRP.
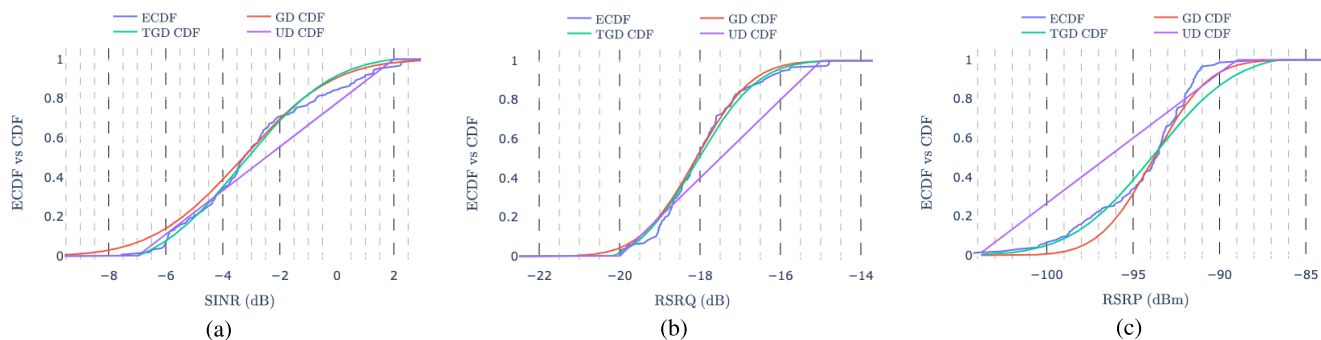

FIGURE 3. Omni-directional antennas ECDF at 100 m AGL compared with the CDFs of GD, TGD, and UD, of: (a) SINR, (b) RSRQ and (c) RSRP.

are used. Therefore, when all subcarriers are used, it follows:

$$S_{\text{tot}} = 12 \cdot N_{\text{PRB}} \cdot RSRP. \qquad (6)$$

By substituting Eq. (6) into Eq. (4), it is possible to obtain

$$SINR = \frac{12 \cdot N_{\text{PRB}} \cdot RSRP}{I_{\text{tot}} + N_{\text{tot}}}. \qquad (7)$$

Then, by substituting Eq. (1) at the denominator, it is possible to rewrite the SINR as

$$SINR = \frac{12 \cdot N_{\text{PRB}} \cdot RSRP}{RSSI - S_{\text{tot}}}. \qquad (8)$$

Using again Eq. (3) for the RSRP and Eq. (6) for N_{PRB}, from Eq. (8) one finally obtains

$$SINR = \frac{1}{\frac{1}{12 \cdot RSRQ} - \frac{N_{\text{RE}}}{N_{\text{PRB}_{\text{used}}}}}. \qquad (9)$$

To summarize: the RSRQ can be derived from the measured values of RSSI and RSRP; the SINR can be derived from the RSRQ. The considered signal quality metrics have been measured at five different UAV flight altitudes, namely 20, 40, 60, 80 and 100 m. The Empirical Cumulative Distribution Functions (ECDFs) of the measured values are shown in Figure 2. More precisely, the ECDF of the SINR is shown in Figure 2(a), the ECDF of the RSRQ is shown in Figure 2(b), while the ECDF of the RSRP is shown in Figure 2(c). As can be observed from the obtained results, the higher the flight altitude, the lower the 4G LTE radio

TABLE 1. Statistical parameters adopted in the CDFs of the chosen probability distributions.

	GD	TGD	UD
SINR	$\mu = -3.5$ dB $\sigma = 2.5$	$\mu = -3.5$ dB $\sigma = 2.5$ $a = -7$ dB $b = 3$ dB	$a = -7$ dB $b = 3$ dB
RSRQ	$\mu = -18.1$ dB $\sigma = 1.2$	$\mu = -18.1$ dB $\sigma = 1.3$ $a = -20$ dB $b = -15$ dB	$a = -20$ dB $b = -15$ dB
RSRP	$\mu = -93.8$ dBm $\sigma = 2.5$	$\mu = -93.8$ dBm $\sigma = 2.5$ $a = -104$ dBm $b = -89$ dBm	$a = -104$ dBm $b = -89$ dBm

signal quality indexes values (than those observed at the ground level). This leads to a decrease of the network's effective performance and stability, thus hindering the safety of BVLOS missions.

For the sake of completeness, it is useful to compare the ECDFs of the measured values to the CDFs of classical probability distributions [8]. More in detail, we compare the ECDFs obtained at 100 m AGL flight altitude with the CDFs of the following three classical distributions—a graphical comparison (in terms of experimental results) is shown in Figure 3, with the ECDF and CDFs of SINR, RSRQ, and RSRP being shown in Figure 3(a), Figure 3(b), and Figure 3(c), respectively, while their corresponding parameters, chosen on the basis of an experimental tuning, are listed in Table 1 (for clarity reasons).

- Gaussian Distribution (GD): a GD $\mathcal{N}(\mu, \sigma^2)$ is characterized by the following Probability Density

Function (PDF) [8]:

$$\phi\left(\mu, \sigma^2; x\right) = \frac{1}{\sigma\sqrt{2\pi}} e^{-\frac{1}{2}\left(\frac{x-\mu}{\sigma}\right)^2} \quad (10)$$

where μ and σ are the average value and the standard deviation. In particular, μ represents the average value of the specific measured radio quality index (namely, SINR, RSRQ or RSRP). To this end, the following parameters have been selected, by trial and error, for each radio quality index:

– in the case of SINR (shown in Figure 3(a)): $\mu = -3.5$ dB, $\sigma = 2.5$;
– in the case of RSRQ (shown in Figure 3(b)): $\mu = -18.1$ dB, $\sigma = 1.2$;
– in the case of RSRP (shown in Figure 3(c)): $\mu = -93.8$ dBm, $\sigma = 2.5$.

• Truncated Gaussian Distribution (TGD): the TGD [8] can be derived from an initial GD $\mathcal{N}(\mu, \sigma^2)$ by truncating it over the interval $[a, b]$. Its corresponding PDF thus becomes:

$$\psi(\mu, \sigma^2, a, b; x)$$
$$= \begin{cases} 0 & \text{if } x \leq a \\ \dfrac{\phi\left(\mu, \sigma^2; x\right)}{\Phi\left(\mu, \sigma^2; b\right) - \Phi\left(\mu, \sigma^2; a\right)} & \text{if } a < x < b \\ 0 & \text{if } x \geq b. \end{cases}$$
$$(11)$$

where: μ represents the average value of the specific measured radio quality index; σ^2 is the variance; and the interval $[a, b]$ has been selected according to the measurement interval ranges experienced during the flying survey. The following parameters have been adopted, by trial and error, for each radio quality index:

– in the case of SINR (shown in Figure 3(a)): $\mu = -3.5$ dB, $\sigma = 2.5$, $a = -7$ dB, $b = 3$ dB;
– in the case of RSRQ (shown in Figure 3(b)): $\mu = -18.1$ dB, $\sigma = 1.3$, $a = -20$ dB, $b = -15$ dB;
– in the case of RSRP (shown in Figure 3(c)): $\mu = -93.8$ dBm, $\sigma = 2.5$, $a = -104$ dBm, $b = -89$ dBm.

• Uniform Distribution (UD): a UD $\mathcal{U}[a, b]$ is characterized by the following PDF [8]:

$$f(x) = \begin{cases} \dfrac{1}{b-a} & \text{for } a \leq x \leq b \\ 0 & \text{for } x < a \text{ or } x > b \end{cases} \quad (12)$$

where the interval $[a, b]$ has been selected according to the interval of the measurement ranges obtained during the flying survey. To this end, the following parameters have been adopted for each radio quality index:

– in the case of SINR (shown in Figure 3(a)): $a = -7$ dB, $b = 3$ dB;
– in the case of RSRQ (shown in Figure 3(b)): $a = -20$ dB, $b = -15$ dB;

TABLE 2. Comparison of the results of the KS test with respect to the ECDF.

Quality Index	Distribution	KS Statistic	KS P-Value
SINR	GD	0.073	0.816
	TGD	0.054	0.872
	UD	0.187	0.011
RSRQ	GD	0.053	0.894
	TGD	0.044	0.925
	UD	0.280	$1.39 \cdot 10^{-5}$
RSRP	GD	0.133	0.139
	TGD	0.088	0.241
	UD	0.233	$5.41 \cdot 10^{-4}$

– in the case of RSRP (shown in Figure 3(c)): $a = -104$ dBm, $b = -89$ dBm.

According to the results shown in Figure 3, it can be concluded that the ECDFs are best approximated by the TGD. In Table 2, we report the Kolmogorov–Smirnov (KS) test [9] statistic and its P-value between the ECDF and the CDFs of the considered classical probability distributions. The results of the KS test confirm that the best fitting distribution is the TGD, returning the highest KS P-value and the lowest KS statistic. This can be explained by the fact that TGD allows to truncate the GD to the boundaries of the measurement range of the used modem (e.g., signal quality indexes cannot exceed above and below a certain threshold), thus better approximating the ECDF.

III. RELATED WORK

Several literature works carried out in-flight measurement, like the one presented in Section II, with the aim to verify the feasibility of cellular connectivity (4G and, recently, 5G) for UAVs.

In [10], 4G LTE signal behaviour data from a UAV-mounted cellular modem are collected, obtaining (similarly to the results shown in Figure 2) a decrease of the main radio quality indexes at higher altitudes. The authors conclude that higher levels of interference incoming from the neighboring cells (due to their signals' free-space propagation) lead to an average 5 dB Signal-to-Interference-plus-Noise Ratio (SINR) degradation with respect to ground-located cellular equipment.

In [11], results coherent with ours are obtained in different environments, while the overall limits of existing 4G LTE cellular networks are also underlined in [12]. A similar investigation has been carried out in [13], confirming that: (i) at altitudes higher than 100 m AGL, the free-space path loss of radio signals transmitted by nearby cell towers, combined with the antennas side-lobes of the BTSs, can significantly degrade the performance quality and reliability of existing 4G LTE networks for aerial connected UAVs; and (ii) increasing the flight altitude, the cell association patterns become more complex, thus afflicting the network stability.

In order to overcome these problem in deploying 4G LTE cellular connected UAVs, the 3rd Generation Partnership Project (3GPP) Release 15 [14] introduced enhancement aiming at mitigating the interference problem [15], [16].

However, despite technical studies and proposed interference mitigation approaches, it is concluded that assumptions, models and techniques used in the design and deployment of cellular networks need to be revised, and that only newer generation of cellular networks (e.g., 5G and 6G) might satisfy them.

In [17], an analysis of the neighboring cells interference problem and a model for aerial cellular connectivity are presented, together with two possible solutions to make existing 4G LTE cellular networks more reliable: (i) the use of directional antennas mounted on a UAV and (ii) the use of interference cancelling techniques. With regard to the *first* solution (similar to the SSAS proposed in this paper), the adoption of 2, 4, and 6 directional antennas has been evaluated through a simulator, showing promising results for increasing number of directional antennas. However, there is no experimental validation through physically deployed systems. Another three-dimensional network simulator for connected UAVs is proposed in [18] suggesting (through extensive numerical results) the use of directional antennas mounted on the UAV to possibly mitigate interference problems. Another 3D model to estimate 4G LTE cellular network performance for connected UAV is proposed in [19], in the end suggesting the use of millimeter waves (mmWaves) to overcome and control the interference on newer generation cellular networks, but lacking the applicability to existing 4G LTE networks. An alternative approach not relying on *on-board* directional antennas is proposed in [20], where the UAV's path is planned on the basis of the radio signal quality, thus ensuring a higher connectivity reliability. However, this approach requires the definition of a radio map, built through filed measurements, and cannot always be applied, since for some specific flight missions it is not possible to change the flight path and/or to know the radio map in advance.

Multiple antenna systems have been investigated to transmit and receive the signal only from the intended direction, which varies over time depending on the relative orientation of the UAV and the base station [21], [22], [23]. These systems include a number of radiating elements arranged on a 3D surface and a feed network, used to activate the optimal radiating elements to support the communication link.

In [21], a review of patch antennas used for UAV-borne systems, where the need of 360° beam coverage at relatively high gain is addressed, is presented, then identifying multiple switched patch antennas and phased array patch antennas as valuable solution for this problem. In [22], a system composed by five dual-port dual-polarization crossed inverted-V antennas optimized for UAV *Air-to-Ground* communication is proposed, where the feed network is based on a Single-Pole-Five-Throw (SP5T) switch (antenna selection) and five Single-Pole-Double-Throw (SP2T) switches (polarization selection). The system is designed to operate in the frequency band from 5.5 GHz to 5.9 GHz, and has been tested in the field with Continuous Wave (CW) signals, using a portable spectrum analyzer as ground base receiver. In [23], a beam
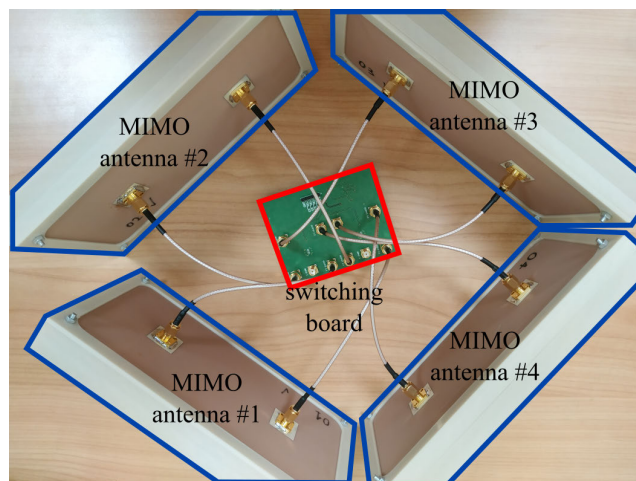

FIGURE 4. Complete antenna system (top view): switching board and four 2 × 2 MIMO directional antennas.

switched antenna system for UAV-to-UAV communications with 360° beam coverage and dual polarization is presented, in detail with the system being based on a 16 Yagi-Uda planar dipole array, and with single antenna elements being able to operate in the frequency band from 4.9 GHz to 6.1 GHz. Then, a cellular modem has been used to connect to a real LTE cellular network. Moreover, the experimental evaluation in [22] has been conducted with the UAV at fixed height and position, while the ground base receiver is placed in different positions. Similarly, the antenna system in [23] has been tested with CW transmitted signal only in laboratory conditions, at a distance between transmitter and receiver equal to 25 cm.

IV. SYSTEM ARCHITECTURE

The proposed SSAS has been defined for enabling re-configurable directional communication and is composed by four main components:

(i) four directional 2 × 2 MIMO antennas, detailed in Subsection IV-A and properly designed to minimize their weights and optimized for LTE networks' frequency range—LTE Band 3 (1710 ÷ 1880 MHz) and LTE Band 7 (2500 ÷ 2690 MHz);

(ii) a switching network, detailed in Subsection IV-B, which the four antennas, the cellular modem, and the control wires are connected to;

(ii) the LTE cellular modem, detailed in Subsection IV-C and connected to the *on-board* processing module which, in turn, communicates with the UAV's Flight Controller (FC) to retrieve telemetry data;

(iv) the antennas control algorithm, described in Subsection IV-D and executed in real-time at the processing module for controlling the antennas' switching network on the basis of different selection criteria.

In the following, a detailed description of each SSAS component will be done.
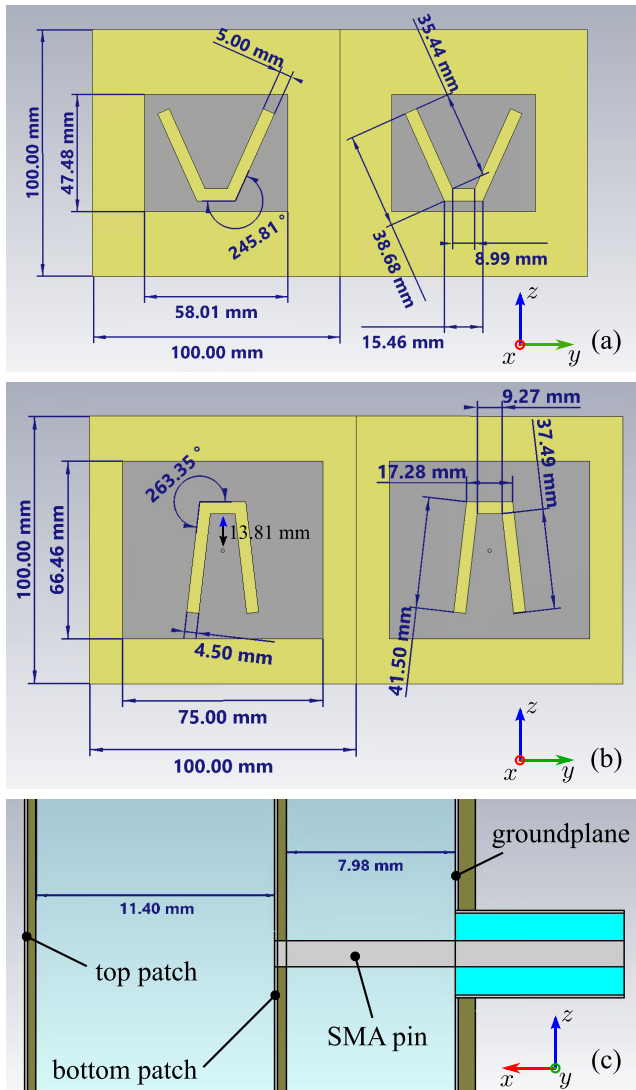
FIGURE 5. 2 × 2 MIMO antennas layout: (a) top patches, (b) bottom patches, (c) distance between the two patches layers made of FR4 with 0.4 mm thickness, and distance between the bottom patch and the ground plane (FR4 0.8 mm with metallization). The two patches are spaced 100 mm.

A. 2 × 2 MIMO DIRECTIONAL ON-BOARD ANTENNAS

The SSAS is equipped with four 2 × 2 MIMO directional antennas oriented in four different directions. The array includes 8 stacked rectangular patch antennas, arranged in pairs at the four sides of a cube to provide a 360° coverage on the azimuthal plane. The antenna system is shown in Figure 4. The antennas are designed in planar technology as grounded stacked V-slotted patches, as shown in Figure 5. This antenna type allows one to cover one quarter of the azimuthal plane, while reducing backlobe radiation owing to the presence of a ground plane. More in detail, each radiating element consists of three layers, each manufactured on a 0.4 mm FR4 substrate ($\epsilon_r = 4.77$, loss tangent 0.011). The three layers are separated using a 3D printed frame. The gap between the first V-slotted patch (bottom patch) and the ground plane is 7.98 mm. The distance between the second patch (top patch) and the first
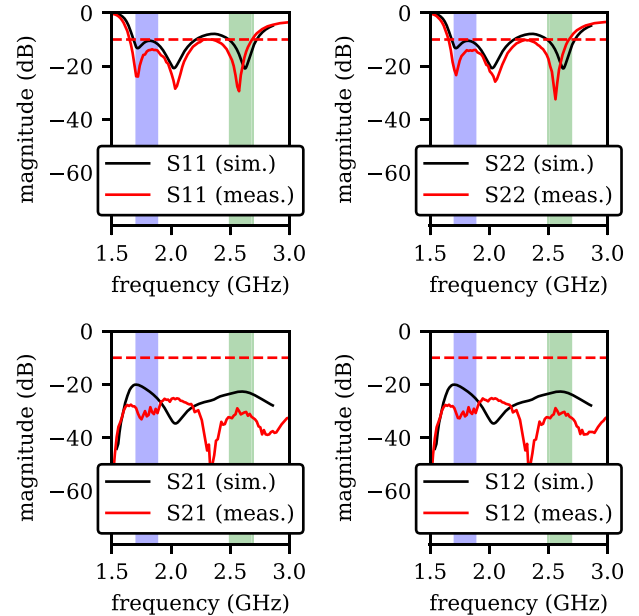

FIGURE 6. Measurement of S-parameters of the realized 2 × 2 MIMO antenna, with bandwidths of interest and the −10 dB level (highlighted).

patch is 11.40 mm. The metallization thickness is 35 μm. The dimension of each antenna panel (2 elements aligned horizontally, at a 10 cm distance), including the 3D-printed frame, is equal to 21 × 11 × 2.4 cm. Eventually, the weight is 0.153 kg per antenna.

The S-parameters of one of the implemented antennas are shown in Figure 6. In this measurement, the single radiating elements of each 2×2 MIMO antenna are connected to a 2-port VNA. The obtained results show that the two radiating elements of the 2 × 2 MIMO antenna are matched. The coupling coefficient between the two antennas is below −25 dB throughout the band of interest. The antennas input reflection coefficient is verified to be under 10 dB in the bandwidth of interest. The test was repeated for all manufactured antenna panels. All the realized antennas have shown S-parameters similar to the ones shown in Figure 6.

The radiation patterns of the single radiating element has been measured in an anechoic chamber. The antennas radiation pattern (simulated and measured) at the extremes of the operational band are presented in Figure 10 and Figure 11. Measurements and simulations are in good agreement. The antennas show a 3 dB beamwidth that decreases monotonically from 80° at 1.71 GHz to 60° at 2.69 GHz on the H-plane, with the main lobe horizontal direction varying between +5° and −7° with respect to the boresight direction (0°). The 3 dB beamwidth on the E-plane varies from 65° at 1.71 GHz to 56° at 2.69 GHz, with the main lobe vertical direction varying between +5° (uptilt) and −7° (downtilt) with respect to the boresight direction (0°). The realized gain at boresight direction varies between 7.3 dBi and 8.6 dBi in the operational bandwidths. The antennas operates in vertical polarization (the E-plane
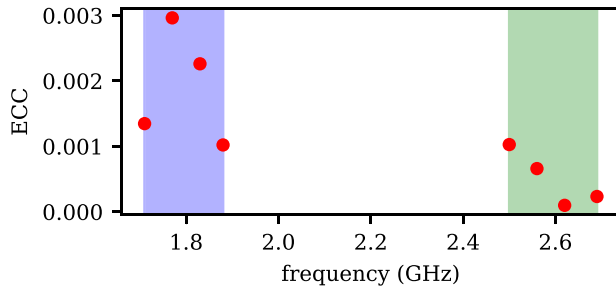
FIGURE 7. ECC in the bandwidths of interest (highlighted).

cross-polar component is more than 15 dB below the co-polar, at the antenna boresigth).

To ensure that the antenna design is suitable for a MIMO telecommunication system, the Envelope Correlation Function (ECC) of this 2 × 2 MIMO antenna has been evaluated from the far-field simulation results with the dedicated tool in CST Studio [24]. The ECC is shown, as a function of the frequency, in Figure 7 and is well below the threshold value of 0.5 (maximum value below 0.003), thus making the designed antennas appropriate for the 2×2 MIMO telecommunication system.

B. SWITCHING NETWORK

The adaptive connection between the modem and the antennas is realized with a pair of Single-Pole 4-Through (SP4T) microwave switches, one per channel of the 2 × 2 MIMO system. The proposed solution is based on RF commercial switches (ADRF5040 from Analog Devices). Figure 8 shows the photo of the feed network, including the schematic of the connections between the ports of the two SP4T switches and the radiating elements. In each antenna panel, one radiating element is connected to one switch, and the other is connected to the other switch. This way, once the direction of the base station is determined, both antennas of the panel covering the detected direction are connected to the modem. The output port of each switch is selected by means of two digital control signals generated by a Raspberry Pi (RPi) Single Board Computer (SBC). Only one port at a time can be selected, according to the values of the input control signals.

The RF switches require positive (+3.3 V) and negative supply voltages (−3.3 V). Since the supply voltage is obtained from the RPi SBC, which can provide only a single-ended voltage (+3.3 V), an additional inverting voltage regulator based on LT1611 from Analog Devices has been designed and implemented on the switching feed network. Since the inverting voltage regulator is of switching type, it has been designed to ensure that the input current at start-up is compliant with the RPi absolute maximum ratings. The ADRF5040 can switch the RF signal between the ports within a maximum delay of 1 μs. The output port of the switch is selected with two GPIO pins of the RPi, connected directly to the two control pins of the switch IC interface.
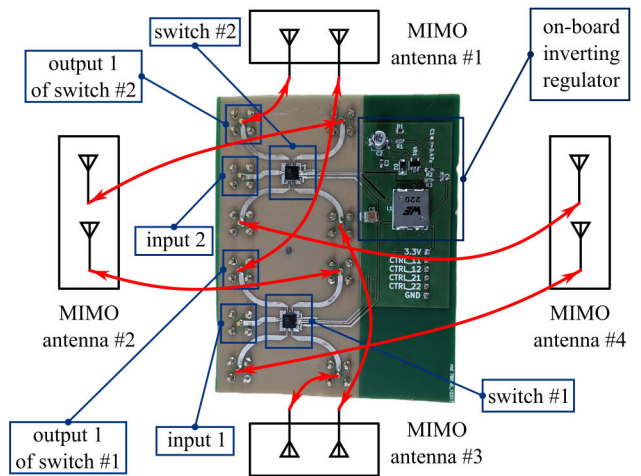

FIGURE 8. Block diagram of the antenna system and switching network PCB. The SMA connectors of the switching board are on the opposite side of the PCB. Red arrows indicate connections between the switching board and the antennas, made with coaxial cables.

The switching board is realized on a FR4 substrate, with a thickness of 0.8 mm. The lines are designed for an impedance of 50 Ω. The transmission lines are designed as short as possible to minimize the losses due to the FR4 substrate, and the lines are distanced as much as possible to minimize coupling between the output ports of the switch. A tapered transition is used to adapt the line width to the pin size of the switch IC.

The S-parameters of the realized switching board have been measured by means of a 2-port VNA. The input of the switch under test is connected to port 1 of the VNA, while port 2 of the VNA is connected to one of its four output ports. In this way, S_{21} and S_{12} represent the losses of the selected path, S_{11} is the reflection coefficient seen from input port of the switching board, while S_{22} is the reflection coefficient at the output port under test of the switching board. For demonstration purposes, Figure 9 shows the measured S-parameters when port 2 of the VNA is connected to output port 1 of one of the SP4T.

The two graphs show the difference between the case in which output port 1 of one of the SP4T is enabled or disabled, while VNA port 2 is still connected to output port 1 of the SP4T. The SP4T ports are labeled in Figure 8. The insertion loss varies from 1.0 dB to 1.3 dB in the frequency band of interest. On the other hand, when output port 2 is enabled and, therefore, port 1 is disabled, the isolation has a value between 35.1 dB and 31.3 dB in the band of interest.

Comparable results are obtained for all the other ports and for the second RF switch. After this characterization, the switching board is considered correctly operational, since it can redirect the input to one of the four output ports without significant losses and without coupling issues with the other ports.

C. UAV PLATFORM

As shown in Figure 12, all the components of the SSAS have been integrated on a custom-built UAV, based on the
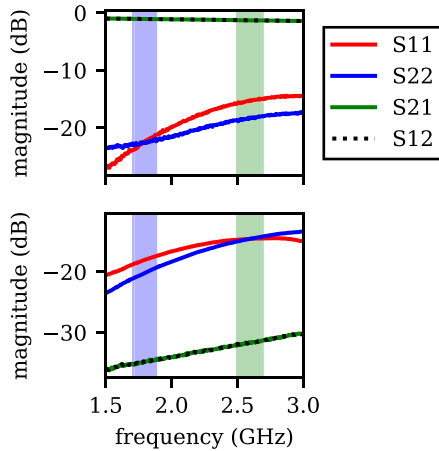
FIGURE 9. Measured S-parameters of the switch network: in the upper part, port 2 of the VNA port 2 connected to output 1 of the switch, while it is enabled. In the lower part, port 2 of the VNA port 2 is connected to output 1 of the switch, while the output 2 is enabled, and therefore output 1 disabled. Bandwidths of interest are highlighted.

Tarot 650 frame, with a customized antennas' support located at the bottom side of the UAV (between its legs, to lower the barycenter of the drone for an improved stability). The four 2 × 2 MIMO antennas have been fixed on a wood basement with a 45° shift with respect to the drone's head, aiming at removing the (possible) interference introduced by the carbon fiber legs of the UAV. Then, the antennas have been connected to the switching network, in turn connected to the Sierra Wireless EM9191 [25] modem's AUX and MAIN antennas' connectors. Finally, the Sierra Wireless EM9191 modem has been connected on top of a proper Techship MU201 [26] M2-to-USB3 adapter providing both power and signal connections required to interface the cellular modem to the *on-board* processing module, based in the first prototypical deployment on a RPi4. Then, the RPi4 has also been connected to the drone's FC, a Pixhawk Cube Orange [27], through a USB cable, thus enabling the main telemetry data retrieval from the FC (with a 10 Hz refresh rate) through the Mavlink [28] communication protocol. Moreover, the RPi4 has been also connected to the four input pins of the antennas' switching network: this allows, through proper HIGH and LOW voltage signals, to enable and disable each antenna according to the chosen antennas control algorithm (detailed in Subsection IV-D). Finally, in order to provide a proper voltage level to the SSAS, a voltage converter connected to the UAV's battery has been used.

D. ANTENNAS CONTROL ALGORITHMS

The performance of the proposed SSAS is evaluated using two different antenna selection algorithms, namely: (i) nearest BTS (NBTS) selection algorithm, detailed in Subsection IV-D1; and (ii) connected BTS (CBTS) selection algorithm, discussed in Subsection IV-D2. The aim is to evaluate and compare the performance obtained by the SSAS (with the two proposed antenna selection algorithms) with

that achieved with the (standard) omni-directional antenna provided by the Sierra Wireless EM9191 cellular modem manufacturer—in the following denoted as Omni-directional BTS (OBTS) antenna selection algorithm. The COTS antenna provided by Sierra Wireless has a gain between 3 dBi and 5.8 dBi, over the bandwidth of interest, and operates with a vertical polarization. The two designed antenna selection algorithms have been evaluated according to the methodology detailed in Section V. However, as will be detailed in the following, the two solutions exploit different antennas' control criteria which, according to the flight altitudes, have different impact on the performance, since the signal propagation of cellular network is heavily affected by the environment and presence of obstacles. Therefore, the performance of both antenna selection algorithms need to be evaluated in order to determine the most effective solution for the proposed SSAS.

1) NEAREST BTS (NBTS) ANTENNA SELECTION ALGORITHM
The NBTS antenna selection algorithm takes into account three main parameters: (i) the location of the *in-flight* UAV, based on its Global Navigation Satellite System (GNSS) coordinates; (ii) the flight direction of the UAV (also denoted as heading angle); and (iii) the location of the nearest BTS, represented by its GNSS coordinates. More in detail, as shown in Figure 13, once the SSAS obtains the telemetry data from the FC, it first loads the data on the known BTSs' location database. Then, after a filtering operation based on the geographical distance between the drone and each BTS (based on their GNSS information), computed through the great-circle distance estimation provided by the Python library GeoPy [29], the UAV internally keeps the list of the only BTSs within a radius of 20 km, in order to speed up the subsequent look-up iterations. Hence, once the nearest BTS has been selected, the NBTS algorithm calculates the bearing angle between the UAV's GNSS coordinates and those of the selected nearest BTS.

More in detail, the bearing angle between UAV and BTS, denoted as θ and expressed in radians (then further converted in degrees), can be calculated according to [30]:

$$\Delta\lambda = \lambda_2 - \lambda_1$$
$$y = \sin(\Delta\lambda) \cdot \cos(\phi_2)$$
$$x = \cos(\phi_1) \cdot \sin(\phi_2) - \sin(\phi_1) \cdot \cos(\phi_2) \cdot \cos(\Delta\lambda)$$
$$\theta = \arctan2(y, x)$$

where: (ϕ_1, λ_1) and (ϕ_2, λ_2) are the two GNSS coordinates, with $\{\phi_i\}_{i=1}^2$ and $\{\lambda_i\}_{i=1}^2$ representing latitudes and longitudes, respectively; $\Delta\lambda$ corresponds to the difference between the longitudes of two coordinates; x and y are intermediate support values used for the computation.

Finally, exploiting (i) the UAV's heading angle and (ii) the bearing angle of the nearest BTS, the NBTS algorithm selects the antenna (out of the four 2 × 2 MIMO antennas available on board) pointing toward the nearest BTS, while the remaining ones remain disabled. As a final remark,
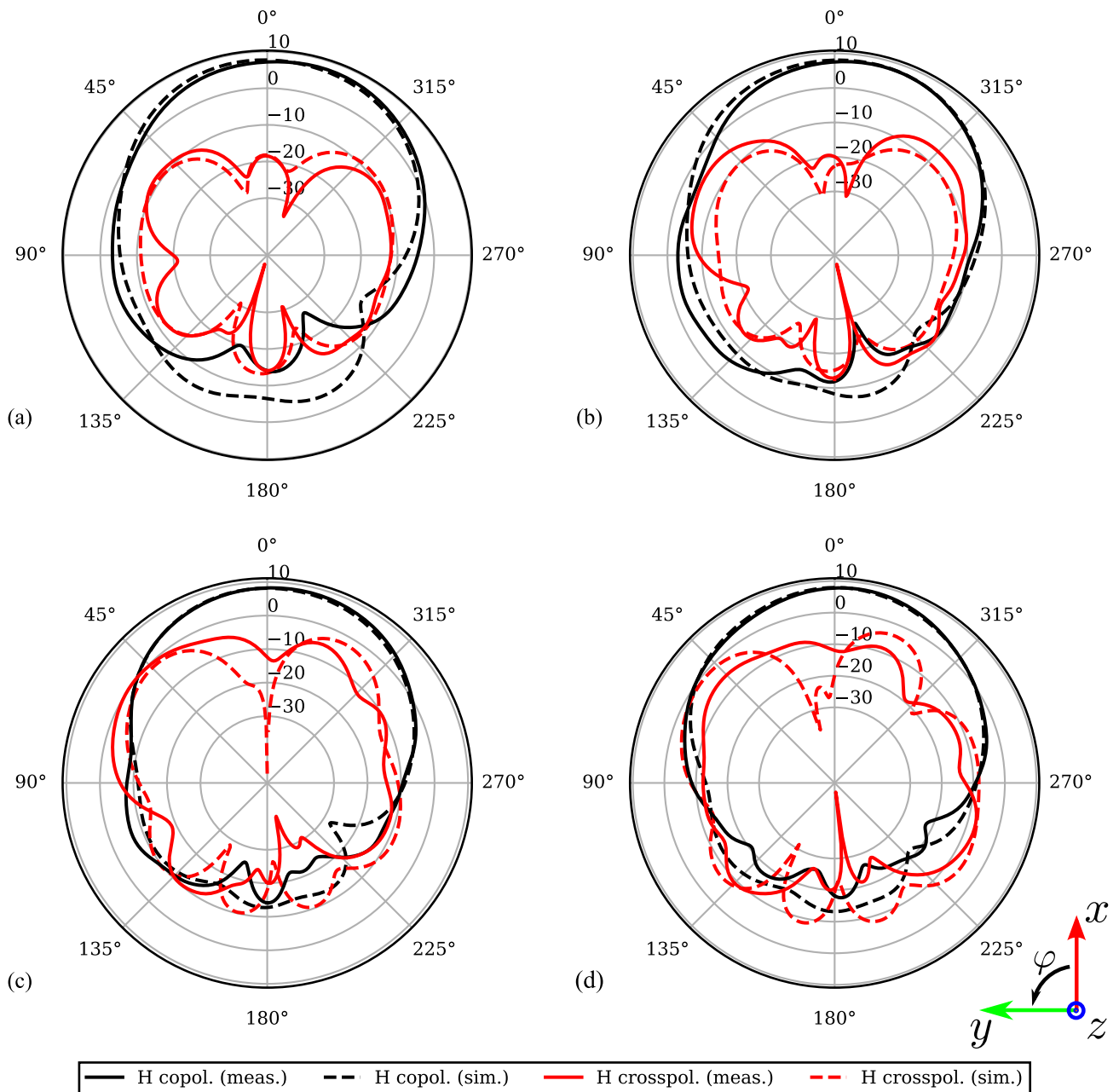
FIGURE 10. H-plane radiation patterns of single antenna element, simulated and measured: (a) 1.71 GHz, (b) 1.88 GHz, (c) 2.50 GHz, (d) 2.69 GHz.

a check on the drone's heading and position is performed every 500 ms, to avoid a fast antenna switching caused by fast UAV's yaw movements affecting the system's stability.

2) CONNECTED BTS (CBTS) ANTENNA SELECTION ALGORITHM

Similarly to the NBTS algorithm detailed in Subsection IV-D1, the CBTS antenna selection algorithm takes into account, as input parameters: (i) the GNSS location of the UAV; (ii) its heading angle; and (iii) the GNSS information of the BTS the LTE modem is connected to. As for the NBTS algorithm,

an initial temporary BTS selection is performed to select only the BTSs located within a distance of 20 km. Then, as shown in Figure 13(b), as soon as the initial cellular network scan is performed, the LTE evolved NodeB (eNB) is retrieved from the collected Cell IDs, as detailed in Subsection V-D, with the SSAS trying to find the BTS with the same eNB in its internal temporary BTSs list:

- if the CBTS algorithm does not find a suitable BTS with the same eNB, then the NBTS algorithm kicks in for this iteration;
- if the CBTS algorithm finds the BTS with the same eNB, then the BTS's GNSS coordinates and data
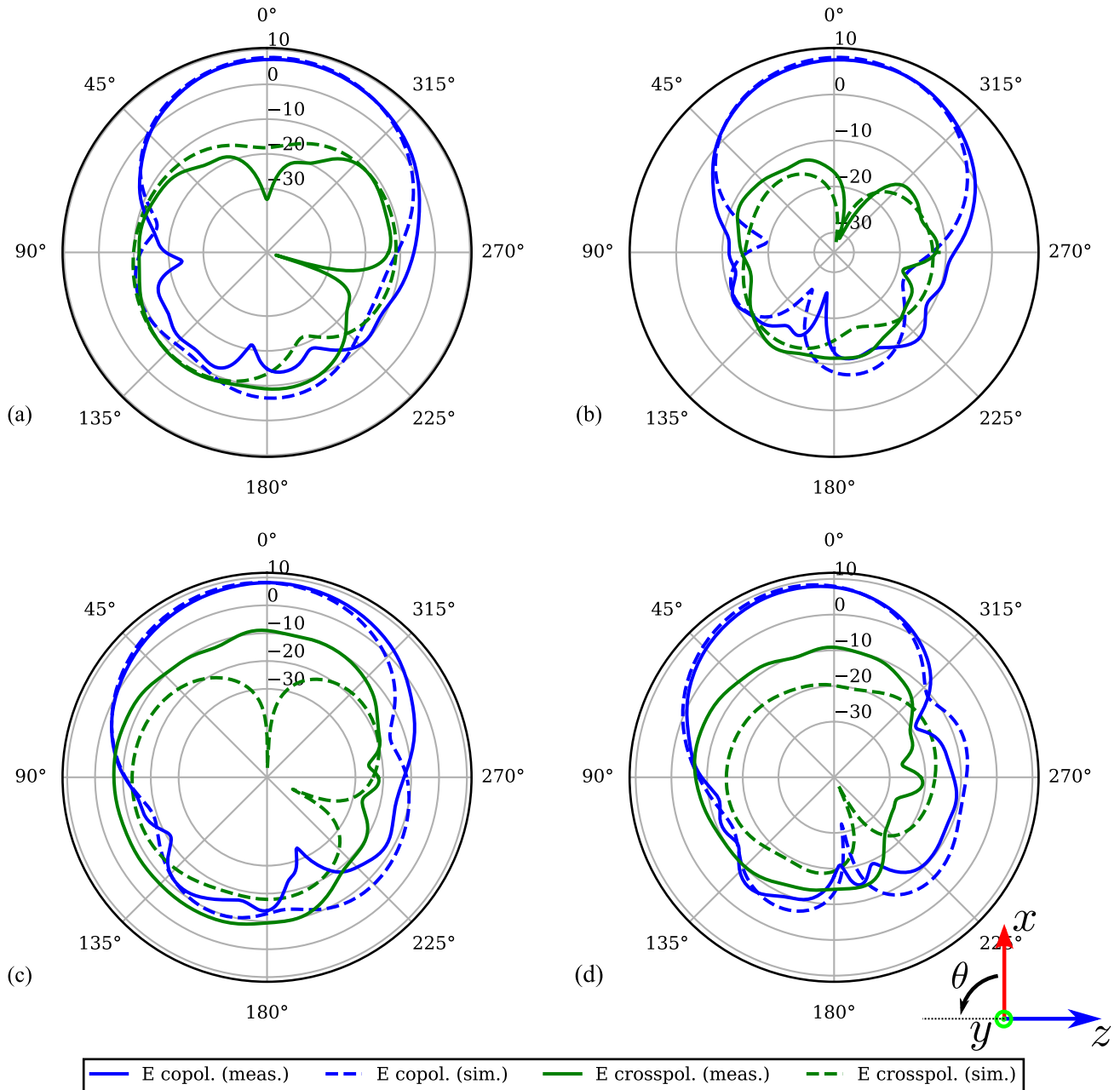
FIGURE 11. E-plane radiation patterns of single antenna element, simulated and measured: (a) 1.71 GHz, (b) 1.88 GHz, (c) 2.50 GHz, (d) 2.69 GHz.

are retrieved, allowing to compute the geographical distance and the bearing angle with respect to the UAV position.

Once the target BTS has been identified, using the drone's heading angle and the computed bearing angle of the connected BTS, it is possible to select the proper 2 × 2 MIMO antenna pointing toward the BTS which the on-board cellular modem is connected to: this antenna is turned *on*, while the other antennas are turned *off*. Finally, as for the NBTS algorithm, a check on the UAV's heading and position is performed every 500 ms.

V. TESTING METHODOLOGY

In order to perform a comparative performance analysis of the proposed SSAS with respect to the omni-directional antenna provided by Sierra Wireless, the following testing methodology has been defined, taking into account several key aspects. In detail, all the experimental measurements have been collected in a known environment (detailed in Subsection V-A), while the UAV FC has been set with the predefined flight path illustrated in Subsection V-B. Then, in order to collect comparable data across several flights, with the considered antennas and antenna selection algorithms, the *on-board*

FIGURE 12. Flying UAV platform used for the flight tests and composed by the drone and the SSAS.

cellular modem's parameters have been set as detailed in Subsection V-C, while gathered radio data are discussed in Subsection V-D.

A. TESTING ENVIRONMENT

The experimental flight tests have been carried out in the Po Valley near Sabbioneta, Mantova, Italy, in a semi-rural area, in order to (i) comply with the EASA regulations and (ii) keep an adequate safety level for both the pilot and the drone during the tests. In particular, this is required since the Maximum Take Off Mass (MTOM) of the UAV (including the SSAS) is around 6 kg, thus not suitable for urban flights over crowded or populated area, where, instead, special permissions and additional safety measures are needed. Moreover, the testing environment features a completely flat terrain—no hills— and allows a direct visibility of tens of BTSs even at a great distance (15+ km). This leads, as shown in the satellite view in Figure 14, to an environment suitable to verify how the proposed SSAS behaves, given the large number of nearby cells available introducing inter-cell interference for the flying drone.

B. FLIGHT PATH

The flight path to be followed by the UAV during the experimental evaluations has been defined and designed targeting the following goals:

- to allow repeatability in the experimental evaluations, so that the drone could easily fly by itself following the predefined (and pre-loaded) flight path several times in order to gather coherent data;
- to collect meaningful results from the experimental evaluations, focusing on the alignment between the UAV's heading and the nearby BTSs (granted by NBTS and CBTS antenna selection algorithms), thus enlighting how effective is switching *on* and *off* the selective and directional antennas to point toward the optimized BTS.

More in detail, the defined flight path requires the UAV to follow a circular path composed by multiple flight points. During the flight, the drone always keeps its heading aligned

with the line tangent to the perimeter of the loop, performing a complete 360° yaw turn during the whole flight. This allows to verify if the proposed algorithms selectively turn *on* the most suitable antennas during the tests (and turn *off* the others). Then, in order to verify the behavior of the proposed SSAS at different flight altitudes, the flight path has been further modified, requiring the UAV to perform multiple overlapped loops but at different flight altitudes, ranging from 20 m AGL up to 100 m AGL, with a 20 m step between consecutive loops. The flight path, composed by five loops at different heights, with 150 measurement points at each height, is shown in Figure 15.

Moreover, the following operational aspects have been considered during the flights:

- the UAV operational mode has been set to AUTO, thus leaving the drone to fly autonomously by following the predefined waypoints;
- the maximum horizontal flying speed has been set equal to 3 m/s, while the yaw speed has been set to AUTO;
- for safety reasons, ascending and descending speeds have been set to a maximum value equal to 2 m/s.

Finally, as will be detailed further in Subsection V-D, the data related to LTE network signals quality indexes, BTS parameters, antennas' selection choice, UAV telemetry, and other flight controller data, have been stored and saved on board the drone, in order to create a complete dataset with multiple flight records.

The same information has been collected, with the same flighr plan, using the omni-directional antenna provided with the Sierra Wireless modem. This allows to experimentally evaluate if the proposed SSAS provides a relevant gain in terms of both signal quality and network stability.

C. NETWORK PARAMETERS

The network parameters adopted in the experiment are detailed as follows. With regard to the cellular network compatibility, the prototypical implementation of the SSAS is mainly suitable only for 4G LTE networks, since the antennas have been designed and tuned to maximize the compatibility with the main LTE bands used by Italian cellular Internet Service Provider (ISPs). Moreover, to minimize the antennas' sizes, the supported frequency range has been narrowed including only 1800 MHz (LTE Band 3: $1710 \div 1880$ MHz) up to 2600 MHz (LTE Band 7: $2500 \div 2690$ MHz), in this way excluding the 800 MHz band (Band 20: $791 \div 862$ MHz). Moreover, the LTE Band 20 has also been neglected for the following reasons.

1) Band 20 is known to support a low throughput, since its useful bandwidth is limited to around 30 MHz, splitted between three operators (10 MHz each). This limits the maximum theoretical throughput to 75 Mbps, lower than the 150 Mbps throughput achievable on Band 3 and Band 7.

2) Band 20 is mainly used in rural areas for indoor coverage, given the higher penetration of radio signal with low carrier frequency. However, since the SSAS
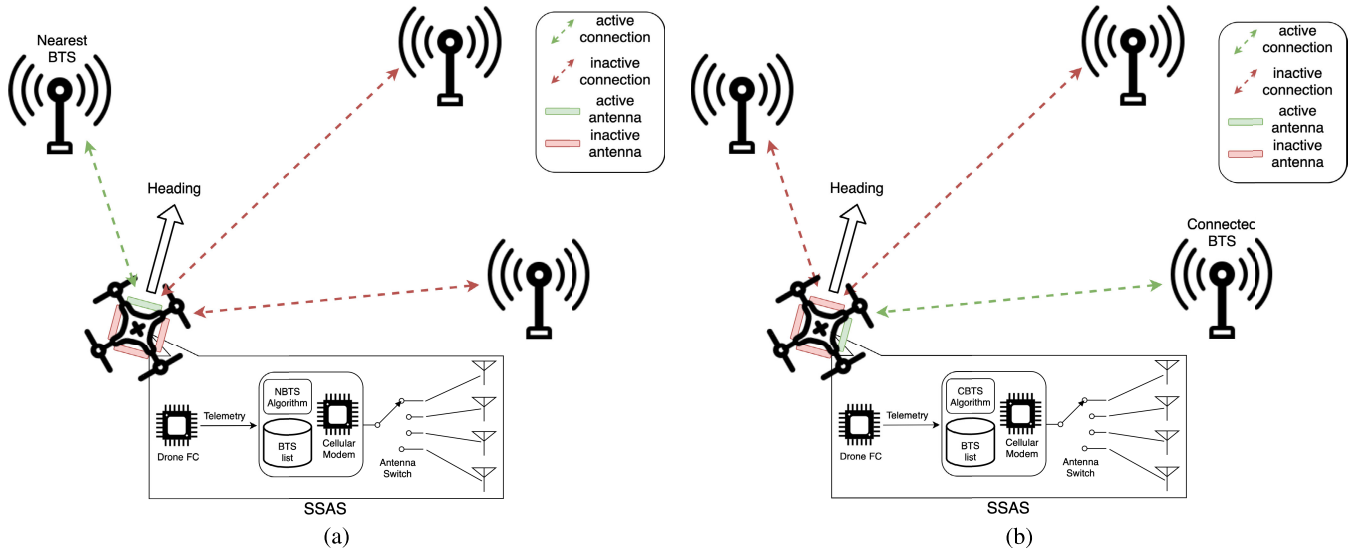
FIGURE 13. Pictorial representation of (a) NBTS algorithm and (b) CBTS algorithm.
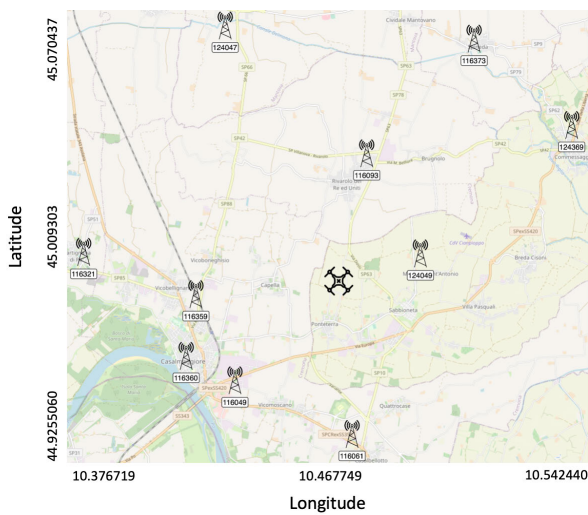

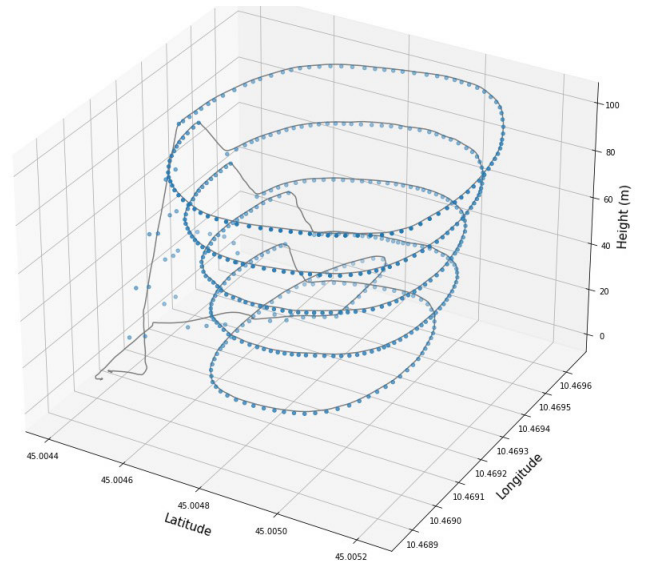**FIGURE 14.** Test environment map with all the eNBs detected by the UAV.

FIGURE 15. Flight path and measurement points used for the data collection.

mainly targets outdoor use cases, mostly in direct LOS conditions between the 4G LTE cellular modem and the eNB, Band 20 can be neglected in favor of the most suitable (and performing) Band 3 and Band 7.

From an implementation persepctive, the SSAS has been designed to satisfy the requirements for LTE Cat. 4 networks. As detailed in Subsection IV-C, it features only 2×2 MIMO channels: therefore, only two antennas' connectors on the EM9191 modem are used (namely, MAIN and AUX connectors), while the other connectors (namely, MIMO1 and MIMO2) are not. Moreover, to avoid bandwidth aggregation (as it is not supported on all the BTSs), the Carrier Aggregation (CA) feature in the EM9191 modem has been disabled, thus making the tests repeatable. Then, in order to gain from more uniform and comparable data collected using both directional (those part of the SSAS) and

omni-directional (e.g., commercial) antennas, the LTE modem has been set: (i) to use only (as anticipated before) the bands within the $1800 \div 2600$ MHz operational range; (ii) to use only 4G LTE networks, thus excluding the use of backward compatible networks (e.g., 2G/3G cellular networks) which share portions of bands in the antennas' frequency operational range.

Despite the compatibility of the adopted EM9191 modem with sub-6GHz 5G networks, experimental evaluations exploiting new generation cellular networks have not been considered mainly for two reasons:

1) 5G networks have not been deployed yet in the rural area where the tests have been performed;

2) the widely used 5G bands, namely Band N78 (3.7 GHz) and Band N28 (700 MHz), are outside of the operational frequency range of the designed directional antennas.

D. IN-FLIGHT DATA COLLECTION PARAMETERS

As anticipated in Subsection V-B, several radio data have been collected and stored inside JSON files during the experimental flights for the evaluation of the aggregated results. In detail, in addition to the 4G radio quality metrics already anticipated indexes detailed in Section III (namely; RSSI, SINR, RSRP, RSRQ), the following parameters (collected every 500 ms from the received radio signals, as mean value, `MAIN` antenna, `AUX` antenna) are considered.

- The LTE Band represents the specific frequency range which 4G LTE signals are transmitted and received within. This range is defined and regulated by regulatory authorities and used by mobile network operators.
- The Cell ID represents a unique identifier assigned to each cell in a mobile network, allowing end devices to recognize and connect to a specific cell.
- The eNB is the key component of 4G LTE BTSs connecting end terminal devices to the core network. Its unique identifier can be computed from the Cell ID value as follows

$$eNB = \left\lfloor \frac{Cell\ ID}{256} \right\rfloor \qquad (13)$$

where the $\lfloor \ldots \rfloor$ denotes the floor function, which rounds the input value down to the nearest integer.

Finally, it is worthy to clarify that: (i) the aforementioned parameters are measured and obtained from the cellular modem located on the UAV, thus being related to the downlink communication link[1] (i.e., from the BTS to the UAV); (ii) data have been associated with the UAV's telemetry data (e.g., GNSS coordinates, altitude information, and other essential data) collected in the same time frame.

VI. EXPERIMENTAL PERFORMANCE EVALUATION

On the basis of the testing methodology detailed in Section V, an experimental performance evaluation of the proposed SSAS is presented and discussed, especially in terms of the network parameters considered in Subsection V-D.

More in detail, in order to get accurate and coherent results, we performed 5 different flights for each system setup of interest, leading to: 5 flights with the omni-directional antenna (denoted, for the sake of comparison, as OBTS); 5 flights with the SSAS running the NBTS as antenna selection algorithm; and 5 flights with the SSAS running the CBTS as antenna selection algorithm. Then, a data pre-processing after each flight was performed, considering as ''valid'' only the data associated with valid telemetry information (e.g., a number of satellites larger than or equal

---

[1]Since we do not have access to the eNB, it has not been possible to measure the same parameters on the BTS side, making it impossible to evaluate the uplink communication quality (i.e., from the UAV to the BTS).

to 6 satellites; valid flight altitude; same LTE band for all the radio data). Finally, the data have been clustered according to their collection flight altitude—considered as a relevant parameter, as it determines the behavior of the cellular network and the overall link quality—and GNSS coordinates, aiming at a position-based comparison between different experimental flights.

In order to evaluate how the antennas' switching mechanisms and the flight altitude affect the LTE cellular network radio signal behaviour during the whole flights (e.g., signal stability and communication link quality), an analysis of the impact of radio and SSAS parameters along the flight path (detailed in Subsection V-B) is discussed in Subsection VI-A. Then, an analysis of the radio parameters, based on clustering the collected data into the five tested flight altitudes, is detailed in Subsection VI-B, while a comparison and evaluation of the impact of the number of eNB changes on the different tested setups and at the various flight altitudes is performed in Subsection VI-C.

A. IMPACT OF THE SSAS CONTROL ALGORITHMS

The first signal behavior analysis has been carried out on the whole flight path followed by the UAV, in order to evaluate how the chosen radio parameters (namely: SINR, RSRQ, RSRP, RSSI, and eNB) evolve as functions of the flight altitude and of the heading angle of the UAV, using both the omni-directional antenna and the proposed multiple antenna system.

The performance of the COTS omni-directional antenna connected to the EM9191 cellular modem located on board the UAV is shown in Figure 16. It is possible to observe that both SINR and RSRQ initially increase and, then, decrease for increasing altitude of the drone, while both RSRP and RSSI drastically increase as soon as the UAV flies a few meters AGL. It can be noticed that, during the flights, SINR, RSRQ, RSRP, and RSSI severely oscillate when the cellular modem connects to a different cell (as represented by the eNB curve). Moreover, while there seems to be a correlation between UAV flight altitude and radio signal quality parameters, no clear correlation can be found between the drone's heading angle and the eNB value: when the drone has the same heading (no matter the flight altitude), the eNB values are often different. The same holds for the radio signal indexes, whose behaviour does not depend on the UAV heading angle, as expected by a system equipped with omni-directional antenna.

The experimental results obtained through the SSAS running the NBTS antenna selection algorithm are shown in Figure 17. It can be seen how the overall behaviour of SINR, RSRQ, RSRP, and RSSI is similar to that obtained with the omni-directional antenna (as a function of the UAV flight altitude), but with the values of the RSRP and RSSI being significantly higher than those shown in Figure 16. On the other end, both SINR and RSRQ are marginally higher than in the case of the omni-directional antenna setup (as further discussed in Subsection VI-B). Moreover, exploiting
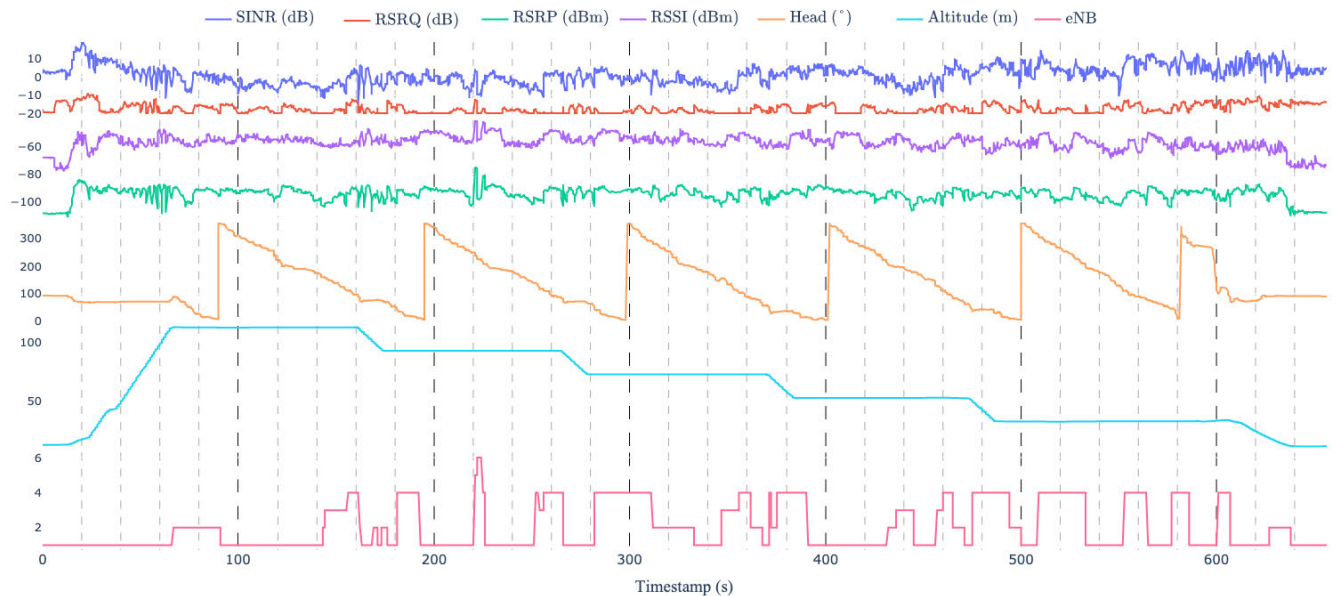
FIGURE 16. Omni-directional antenna LTE radio signal behaviour during the flight at different flight altitudes.

(in Figure 17) the presence of the identifier of the chosen antenna (among the four available on the SSAS), a clear correlation between the chosen antenna and the heading angle emerges. This is due to the fact that the NBTS algorithm enables the antenna aligned with the nearest BTS while the UAV performs its flight mission, slowly rotating on the yaw axis at each flight altitude. For this reason, the selected antenna plot (staircase) line in Figure 17 shows a repetitive pattern correlated to the heading angle, thus confirm that the system is properly working. However, the obtained results show that, despite the directional antenna reduced beamwidth and the use of the NBTS algorithm for proper antenna selection, there are several cell changes, as clearly shown by the eNB curve. To this end, one might expect the system to be able to maintain the connection with the nearest cell without switching to other nearby cells. However, given the significantly higher signal gain of the directional antenna, sometimes the system connects to other cells which are in the same direction towards which the selected antenna is pointing, but often farther away than the nearest one: this explains the lower values of the radio parameters (e.g., as visible at timestamps between 290 and 320). Moreover, if compared to the omni-directional antenna system, in Figure 17 some signal drops can be noticed (e.g., at timestamps 137, 182, 236, 311, 337, and others) when the SSAS switches from one antenna to another—this behaviour will be further discussed in Section VI-D. This will also explain why, even though the average values of the radio parameters are better with the SSAS, the absolute minimum values are with the SSAS that with the omni-directional antenna, as discussed in Subsection VI-B.

Finally, the obtained experimental results with the CBTS antenna selection algorithm are shown in Figure 18. It can be

concluded that RSRP and RSSI values are higher than those obtained with the omni-directional antenna, while a similar signal behavior, as a function of the flight altitude, can be seen in both Figure 16 and Figure 17. In fact, since the CBTS algorithm selects the antenna pointing towards the BTS the modem is connected to, there are no repetitive patterns and no clear correlation between the SSAS antenna identifier and UAV heading angle. However, the same signal drops seen in Figure 17 at the time of antenna switching can be observed in Figure 18 as well: this confirms that antenna switching is the main limitation of the current SSAS implementation.

B. IMPACT OF THE FLIGHT ALTITUDE ON SIGNAL QUALITY

In order to better estimate the SSAS performance (with the antenna selection algorithms detailed in Subsection IV-D) in a comparative way with respect to the omni-directional antenna-based solution, all the data gathered during the various flights, performed for each experimental setup, have been merged into the same dataset[2] (one dataset for each experimental setup). Finally, the obtained datasets have been clustered, *first*, according to the UAV altitude (namely: 20 m, 40 m, 60 m, 80 m, 100 m) and, *then*, according to the GNSS coordinates of the measurement points (e.g., with the same latitude and longitude, with a maximum difference of 1.5 m). More in detail, as detailed in Subsection V-B and shown in Figure 15, 150 GNSS points have been identified and applied to the data clustering function, thus enabling (i) a results' comparison and analysis on the advantages and disadvantages of the proposed SSAS system with respect to the adoption of an omni-directional antenna at different flight altitudes,

[2]The data collected before the test launch and during the altitude transitions were removed to avoid transitories.
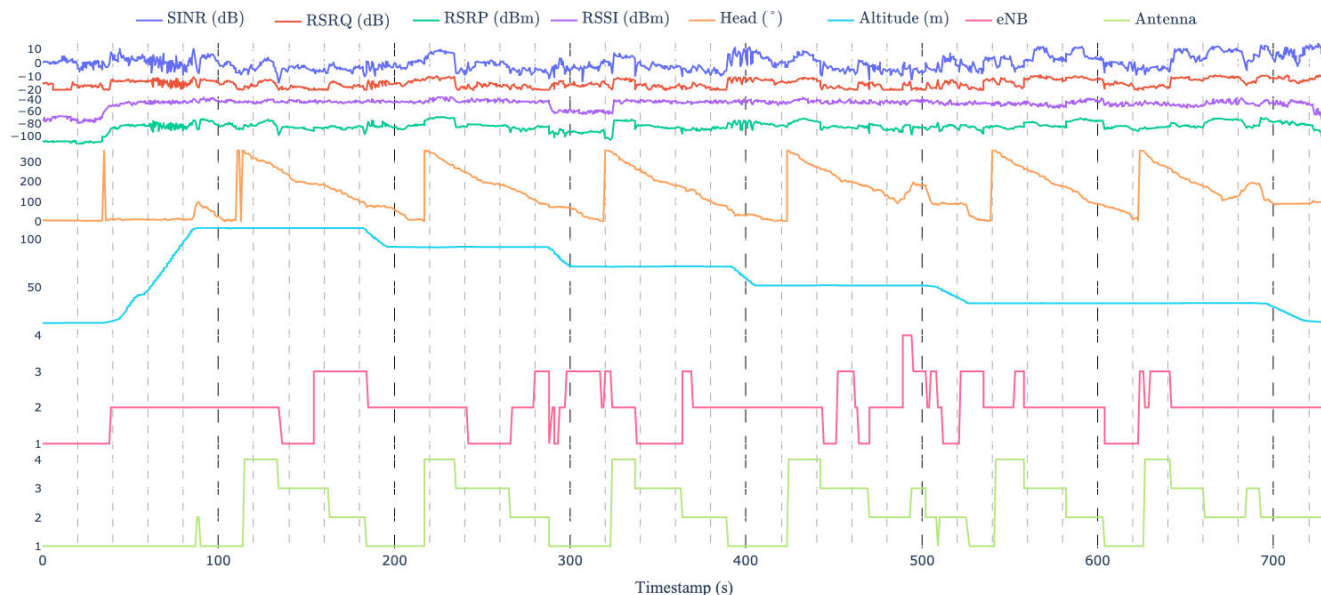
FIGURE 17. Directional antenna with NBTS algorithm LTE radio signal behaviour during the flight at different altitudes.
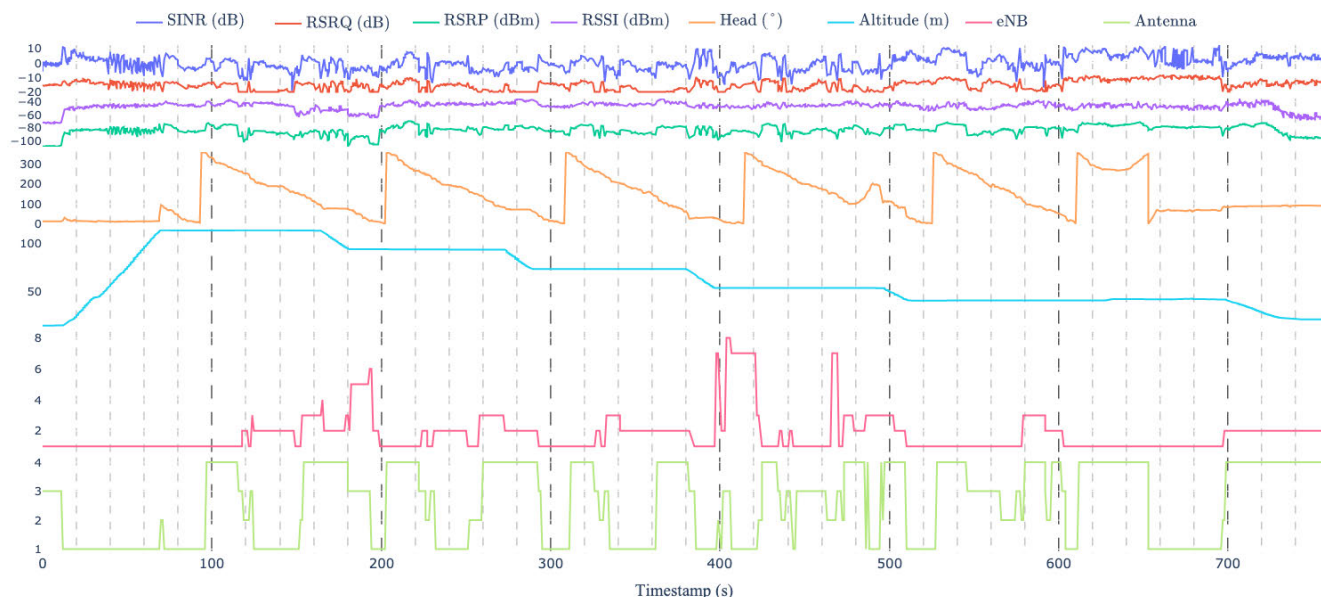

FIGURE 18. Directional antenna with CBTS algorithm LTE radio signal behaviour during the flight at different altitudes.

and (ii) a *one-to-one* comparison between NBTS-, CBTS-, and OBTS-based antenna selection on the basis of the three experimental setups at the same altitude but also at the same GNSS point of the predefined flight path. Moreover, to ease visualization and understanding of the gathered data, the ECDFs of SINR, RSRQ and RSRP have been calculated at the five different flight altitudes.[3] In the following, the main signal quality indexes among the considered experimental

setups (NBTS, CBTS, OBTS) are investigated and discussed at 100 m, 80 m, 60 m, 40 m, and 20 m AGL flight altitudes.

1) EXPERIMENTAL RESULTS AT A 100 M AGL FLIGHT ALTITUDE

The ECDFs of the SINR, RSRQ and RSRP are shown in Figure 19(a), Figure 19(b), and Figure 19(c), respectively. For the sake or completeness, the minimum, maximum, and mean values for all the parameters are listed in Table 3, whose values at a 100 m AGL clearly show an average improvement of RSRP and RSSI when using the SSAS (with both CBTS and NBTS algorithms) with respect to

---

[3]We decided to omit the ECDF of the RSSI since this metric, as discussed in Subsection V-D, is the less relevant, as it measures both the received signal as well as interfering signals. Therefore we focused on the more relevant RSRP to analyze the received signal power.
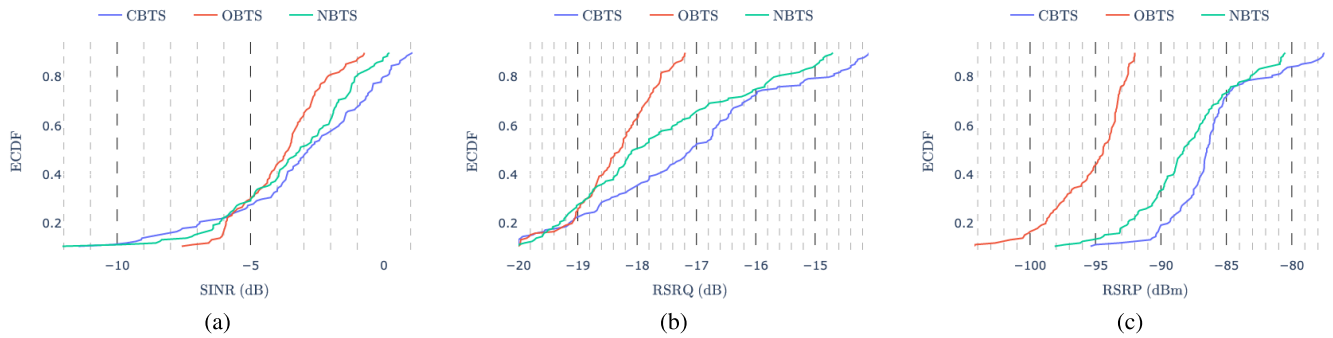
FIGURE 19. (a) ECDF of the SINR among the considered experimental setups (NBTS, CBTS, OBTS) at a 100 m AGL flight altitude, (b) ECDF of the RSRQ among the considered experimental setups (NBTS, CBTS, OBTS) at a 100 m AGL flight altitude, (c) ECDF of the RSRP among the considered experimental setups (NBTS, CBTS, OBTS) at a 100 m AGL flight altitude.

TABLE 3. SINR, RSRQ, RSSI and RSRP measurement at a 100 m AGL flight altitude through the different experimental setups.

	SINR [dB]			RSRQ [dB]			RSSI [dBm]			RSRP [dBm]		
	mean	max	min	mean	max	min	mean	max	min	mean	max	min
CBTS	−1.45	6.95	−11.45	−15.82	−12.35	−20.0	−44.86	−39.38	−54.0	−84.2	−73.75	−95.38
NBTS	−1.97	7.0	−9.85	−16.32	−10.0	−20.0	−46.06	−39.25	−52.88	−85.85	−74.0	−97.38
OBTS	−2.62	3.15	−7.16	−17.87	−14.78	−20.0	−56.24	−52.25	−60.08	−94.33	−89.25	−105.25

the case with omni-directional antenna. In detail, both the average RSRP and RSSI are more than 10 dB higher than the value in the omni-directional antenna case. Regarding the average SINR, both CBTS and NBTS manage to achieve better values, however, for the NBTS the improvement is limited to less than 0.7 dB, while the CBTS manage to achieve a 1.2 dB gain. The same applies to the RSRQ, with the CBTS achieving a gain of almost 2 dB, while the NBTS gain is just 1.5 dB. With regard to the SINR, it must be noticed that the minimum observed values with the SSAS are lower than with the omni-directional antenna. This can be motivated by the signal drops due to the antenna switching, as anticipated in Subsection IV-D1 and as will be further discussed in Subsection VI-D. Overall, from a radio signal quality perspective, at a 100 m AGL flight altitude the best solution seems to adopt a CBTS-controlled SSAS that, on average, returns better radio performance than if controlled through the NBTS algorithm.

2) EXPERIMENTAL RESULTS AT A 80 M AGL FLIGHT ALTITUDE

The ECDFs of the SINR, RSRQ and RSRP are shown in Figure 20(a), Figure 20(b), and Figure 20(c), respectively. Analyzing the obtained results, there is a clear advantage for the SSAS system regarding the RSRP and RSSI, whose values, with the NBTS and CBTS algorithms, are (on average) 10 dB and 6 dB greater, respectively, than those with omni-directional antenna. In this case, the average SINR and RSRQ improvement for the NBTS system is over 2 dB higher than the values with CBTS-based SSAS and with omni-directional antenna, as highlighted by the ECDF shown in Figure 20(a). At a 80 m AGL flight altitude, the NBTS algorithm guarantees the best performance, as shown in Table 4, in which, for the sake or completeness, the minimum,

maximum, and mean values of all the parameters are listed.

3) EXPERIMENTAL RESULTS AT A 60 M AGL FLIGHT ALTITUDE

The ECDFs of the SINR, RSRQ and RSRP are shown in Figure 21(a), Figure 21(b), and Figure 21(c), respectively. At a 60 m AGL flight altitude, the performance gains at the radio level reduce when comparing both the SSAS algorithms (namely, NBTS and CBTS) with the omni-directional antenna system. In detail, the overall gains of the RSRP and RSSI with the SSAS system are within 9 dB and 5 dB, with the NBTS solution achieving the best performance. Regarding SINR and RSRQ, the SINR difference between the three setups is minor, with a 1.5 dB gain of the mean value of the RSRQ in favor of the NBTS, as confirmed by the ECDF shown in Figure 21(a). For the sake or completeness, the minimum, maximum, and mean values of all parameters are listed in Table 5.

4) EXPERIMENTAL RESULTS AT A 40 M AGL FLIGHT ALTITUDE

The ECDFs of the SINR, RSRQ and RSRP are shown in Figure 22(a), Figure 22(b), and Figure 22(c), respectively. Lowering the flight altitude to 40 m AGL, the performance gains of the SSAS further reduce with respect to the case with the omni-directional antenna system. In detail, the main advantages are related to RSRP and RSSI values, given the higher gains of the directional antenna of the SSAS, while the SINR is higher with the omni-directional antenna-based system. The same cannot hold for the RSRQ, which is slightly better on the SSAS controlled by the NBTS algorithm. The overall gains of the RSRP and RSSI are within 5 dB and 3 dB in favor of the SSAS, with NBTS outperforming CBTS. For
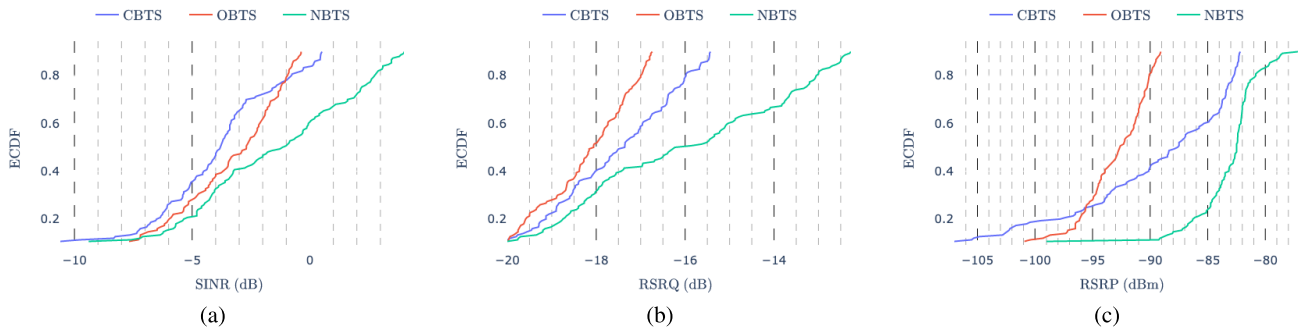
FIGURE 20. (a) ECDF of the SINR among the considered experimental setups (NBTS, CBTS, OBTS) at a 80 m AGL flight altitude, (b) ECDF of the RSRQ among the considered experimental setups (NBTS, CBTS, OBTS) at a 80 m AGL flight altitude, (c) ECDF of the RSRP among the considered experimental setups (NBTS, CBTS, OBTS) at a 80 m AGL flight altitude.

TABLE 4. SINR, RSRQ, RSSI and RSRP measurement at a 80 m AGL flight altitude through the different experimental setups.

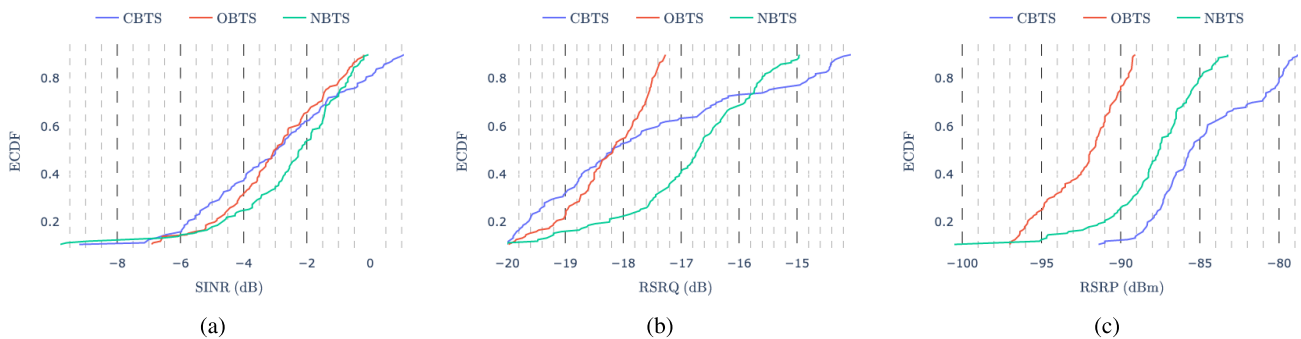|	SINR [dB]			RSRQ [dB]			RSSI [dBm]			RSRP [dBm]		
	mean	max	min	mean	max	min	mean	max	min	mean	max	min
CBTS	−2.88	5.87	−10.6	−16.93	−10.47	−20.0	−47.96	−39.0	−64.5	−87.18	−71.0	−105.5
NBTS	0.35	9.4	−9.3	−15.01	−10.25	−20.0	−43.57	−38.75	−49.5	−80.77	−69.0	−99.0
OBTS	−2.26	3.6	−7.68	−17.74	−15.0	−20.0	−53.5	−47.11	−58.8	−91.72	−84.67	−100.92

FIGURE 21. (a) ECDF of the SINR among the considered experimental setups (NBTS, CBTS, OBTS) at a 60 m AGL flight altitude, (b) ECDF of the RSRQ among the considered experimental setups (NBTS, CBTS, OBTS) at a 60 m AGL flight altitude, (c) ECDF of the RSRP among the considered experimental setups (NBTS, CBTS, OBTS) at a 60 m AGL flight altitude.

TABLE 5. SINR, RSRQ, RSSI and RSRP measurement at a 60 m AGL flight altitude through the different experimental setups.

	SINR [dB]			RSRQ [dB]			RSSI [dBm]			RSRP [dBm]		
	mean	max	min	mean	max	min	mean	max	min	mean	max	min
CBTS	−1.87	7.4	−7.14	−16.82	−12.1	−19.95	−44.1	−38.0	−48.58	−83.09	−73.25	−91.4
NBTS	−1.85	5.9	−13.2	−16.24	−12.15	−20.0	−47.55	−42.0	−55.58	−86.29	−74.5	−103.5
OBTS	−2.27	2.96	−7.58	−17.95	−15.86	−20.0	−53.16	−47.8	−58.67	−91.62	−86.81	−97.42

the sake of completeness, minimum, maximum, and mean values of all parameters are listed in Table 6.

5) EXPERIMENTAL RESULTS AT 20 M AGL FLIGHT ALTITUDE
The ECDFs of SINR, RSRQ and RSRP are shown in Figure 23(a), Figure 23(b), and Figure 23(c). At a 20 m AGL flight altitude, the behaviour of the SSAS is quite similar to that at 40 m AGL, with some relevant gains only for RSRP, RSSI and RSRQ values, while the SINR (shown in the ECDF depicted in Figure 23(a)) with the SSAS does not improve over the omni-directional antenna-based system. The gains of the RSRP and RSSI are within 7 dB and 5 dB in favor of the SSAS, with the CBTS solution achieving the best performance. The RSRQ shows similar values for

CBTS and NBTS solutions, both achieving an average gain close to 1.5 dB with respect to the omni-directional antenna-based solution. For the sake of completeness, the minimum, maximum, and mean values of all parameters are listed in Table 6.

C. IMPACT ON THE AMOUNT OF CELL CHANGES
The last experimental performance evaluation, whose results are shown in Table 8, has been performed investigating the amount of cell changes experienced during the experimental flights—6 flights for each setup—at different AGL flight altitudes.

According to the results listed in Table 8, the proposed SSAS experiences a smaller number of cell changes when
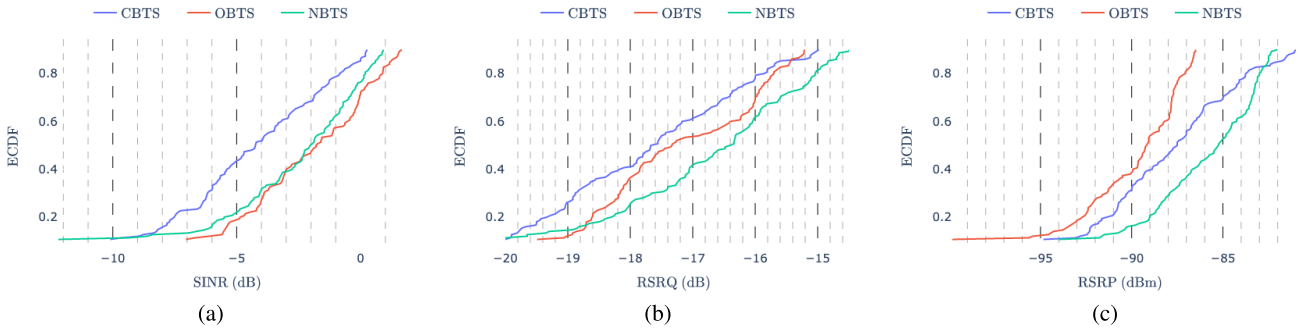
FIGURE 22. (a) ECDF of the SINR among the considered experimental setups (NBTS, CBTS, OBTS) at a 40 m AGL flight altitude, (b) ECDF of the RSRQ among the considered experimental setups (NBTS, CBTS, OBTS) at a 40 m AGL flight altitude, (c) ECDF of the RSRP among the considered experimental setups (NBTS, CBTS, OBTS) at a 40 m AGL flight altitude.

TABLE 6. SINR, RSRQ, RSSI and RSRP measurement at a 40 m AGL flight altitude through the different experimental setups.

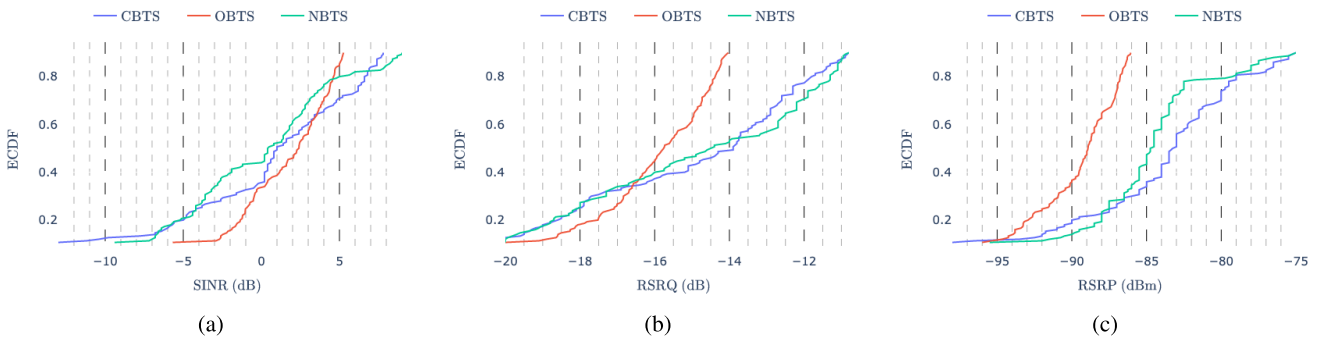|	SINR [dB]			RSRQ [dB]			RSSI [dBm]			RSRP [dBm]		
	mean	max	min	mean	max	min	mean	max	min	mean	max	min
CBTS	−2.86	5.96	−8.93	−16.77	−11.2	−19.9	−46.2	−38.0	−52.69	−85.58	−74.5	−94.83
NBTS	−1.56	4.13	−12.2	−16.06	−12.92	−20.0	−46.12	−41.67	−57.12	−84.53	−76.7	−94.0
OBTS	−0.96	4.9	−7.05	−16.67	−13.4	−19.65	−51.68	−46.5	−61.25	−88.75	−82.5	−102.5

FIGURE 23. (a) ECDF of the SINR among the considered experimental setups (NBTS, CBTS, OBTS) at a 20 m AGL flight altitude, (b) ECDF of the RSRQ among the considered experimental setups (NBTS, CBTS, OBTS) at a 20 m AGL flight altitude, (c) ECDF of the RSRP among the considered experimental setups (NBTS, CBTS, OBTS) at a 20 m AGL flight altitude.

TABLE 7. SSINR, RSRQ, RSSI and RSRP measurement at a 20 m AGL flight altitude through the different experimental setups.

	SINR [dB]			RSRQ [dB]			RSSI [dBm]			RSRP [dBm]		
	mean	max	min	mean	max	min	mean	max	min	mean	max	min
CBTS	2.63	11.2	−13.0	−13.85	−8.9	−20.0	−46.72	−38.5	−53.5	−81.66	−72.0	−98.0
NBTS	1.94	12.0	−9.4	−13.99	−8.8	−20.0	−47.52	−38.5	−54.0	−82.53	−71.0	−94.5
OBTS	2.9	11.5	−4.4	−15.43	−11.95	−20.0	−52.58	−45.0	−57.83	−88.3	−79.5	−95.92

TABLE 8. Amount of network cell changes experienced during 6 experimental flights at different AGL flight altitudes, for the considered experimental setups.

	100 m	80 m	60 m	40 m	20 m
CBTS	36	34	42	63	47
NBTS	32	22	34	48	54
OBTS	49	44	38	31	27

the UAV is at 100 m and 80 m AGL with respect to the omni-directional antenna-based system, with the NBTS algorithm providing the best performance (especially at a 80 m AGL flight altitude). At lower flight altitudes (at 60 m), the performance of the three experimental setups is similar, with a small advantage for the NBTS-based solution.

Instead, at 40 m and 20 m AGL, the omni-directional antenna-based system manages to achieve a sufficiently smaller number of cell changes with respect to the SSAS. In fact, these results reflect those related to the radio quality indexes discussed in Subsection VI-B: the SSAS achieves better performance at higher flight altitudes when the drone is in LOS condition with more BTSs, while the omni-directional antenna-based system, instead, experiences additional interference. On the other side, at lower flight altitudes, the omni-directional antenna-based solution performs better, since more complex factors affect the performance of the cellular network (e.g., signal shadowing and reflections due to trees, buildings and other possible sources of noise).

D. RESULTS DISCUSSION

Looking at the results presented in Subsections VI-A–VI-C, it can be concluded that, as expected, the proposed SSAS provides a signal quality improvement only at high flight altitudes (from 80 AGL to above flight altitudes), where the cellular modem located on board the flying UAV has a higher probability to reach LOS conditions with several BTSs using the same frequency (thanks to the frequency re-utilization scheme of cellular networks highlighted in Figure 1). At lower altitudes, the benefits of the SSAS are negligible, since below 60 m AGL the omni-directional antenna-based system can achieve similar (and even better) results, especially at a 20 m AGL flight altitude, where the LOS condition between the drone and the BTS is no longer guaranteed due to obstacles (i.e., trees, buildings, etc.). This might cause problems in selecting the best serving BTS without knowing the cellular network planning scheme. Therefore, an omni-directional antenna is more suitable for operational applications requiring UAVs flying at smaller flight altitudes. This also explains why, at low altitudes (below 20 m AGL), the best performing SSAS algorithm is the CBTS. However, given the presence of obstacles and, thus, signal shadowing and reflections, the straight line between the UAV and the BTS position does not necessarily represent the strongest propagation path, thus afflicting the reliability and performance of the CBTS-controlled SSAS with respect to the omni-directional antenna-based system.

Looking at the overall SSAS performance, the 2 × 2 MIMO directional antenna design of the proposed system provides significantly higher RSRP and RSSI gains at every flight altitude, with respect to the case with omni-directional antenna. Moreover, their directivity, combined with the proper control algorithm, can improve the SINR and RSRQ at high altitudes. However, as discussed in Subsection VI-A, antenna switching, combined with the non-overlapping beamwidths of the four antennas, introduces signal quality drops, thus lowering the overall performance gain. Despite this drawback, which might be solved with the design of a more advanced switching system (as will be discussed in Section VII), the SSAS can still decrease the overall number of cell changes along the designated flight path, especially at high flight altitudes (where SSAS guarantees the best performance).

Finally, it is interesting to observe that, at most altitudes, NBTS outperforms CBTS. More in detail, at 100 m and 20 m AGL flight altitudes, the best performance is obtained with CBTS, while in all the other cases NBTS is the best. This can be explained by observing that, at different altitudes, there might be different cell signals arriving from nearby BTSs, as shown in [31].

VII. FUTURE IMPROVEMENTS

In order to improve the performance of the proposed SSAS and overcome the drawbacks of the first prototypical version, a few improvements can be identified and applied to the system, on both hardware and software (antenna selection algorithm) sides. In the following, we summarize relevant research directions to improve reliability and performance of the SSAS for complex BVLOS applications.

A. IMPROVED ANTENNAS

A major drawback of the antenna developed in this work is the limitation of the linear polarization. Further developments of the system will focus on developing an antenna with similar bandwidth, gain and weight, but able to operate in dual-polarization, as described in [22] and [23].

B. IMPROVED SWITCHING NETWORK

As highlighted by the experimental evaluation detailed in Section VI, one of the main limitations of the current prototypical SSAS implementation is related to the antennas switching network, which allows to use only one 2 × 2 MIMO antenna at time. This sometimes leads to significant signal drops when the SSAS *hard* switches from one antenna to another. Therefore, in a more advanced version of the system, the switching network should allow the use of multiple antennas at the same time, thus providing the ability to perform a *soft* switch between antennas. As an example, in the case the SSAS system has a specific antenna enabled (e.g., antenna #1) and, given the UAV heading rotation with respect to the target BTS, the SSAS has to switch to the contiguous antenna (e.g., antenna #2), the improved version of the system should activate antenna #2 a few seconds earlier then the switching instant, thus introducing a smoother transition without any signal drop. Moreover, this enhancement could also provide omni-directionality by enabling all four antennas at the same time. This is attractive for low altitude flights, where the current SSAS has a performance worse than the with an omni-directional antenna. The new SSAS should thus make the system more suitable to complete flight missions involving both high and low altitude flight operations.

C. REDUCED SSAS WEIGHT AND SIZES

The currently designed antennas have been optimized in terms of both weight and dimensions for the reference UAV testing platform (detailed in Subsection IV-C). However, targeting the possibility to equip smaller drones with a more advanced deployment of the proposed SSAS, smaller and lighter antennas should be designed, as well as a more compact switching network. Eventually, smaller components would be beneficial not only for smaller drones, but would also allow the integration of additional antennas on the UAV, thus opening to the possibility to more than 2 × 2 MIMO cellular communications (e.g., newer LTE equipment nowadays support up to 4 × 4 MIMO channels).

D. SUPPORT FOR 5G CELLULAR NETWORKS

The current prototypical antennas (detailed in Subsection IV-A) have been optimized for the LTE bands adopted in Italy. However, the SSAS would support, through the use of different antennas, connectivity through different bands,

including the use of the latest 5G cellular networks. Therefore, an enhanced version of the SSAS might include new antennas able to support 5G bands, thus making the SSAS fit for next-generation cellular networks. As a consequence, the same development might hold for other wireless protocols (e.g., Wi-Fi) that could benefit from a re-configurable antennas system such as our proposed SSAS, especially for specific applications where cellular networks may not be available or needed.

E. ENHANCED ANTENNAS CONTROL ALGORITHMS

Finally, on the software side, innovative antennas control algorithms might be designed and integrated in the SSAS, aiming at further optimizing and improving the connectivity performance of the system. As an example, a more robust control algorithm could exploit Machine Learning (ML)-based mechanisms to understand which BTS selection criteria is the most suitable according to various parameters, such as: the flight altitude; the distance between the UAV and the BTSs; and the physical modelling of signal propagation in the different bands, thus allowing a more robust utilization of the SSAS according to the different application scenario.

VIII. CONCLUSION

In this paper, we have presented and discussed the architecture and a prototypical deployment of a SSAS, experimentally evaluated, through different performance campaigns (conducted in an open field in the northern of Italy), in terms of impact of antennas control algorithms, flight altitude on several signal quality indexes, and amount of network cells changes. In detail, we have performed these experimental evaluations on a predefined flight path with a custom-made UAV flying at different flight altitudes (namely: 20 m AGL, 40 m AGL, 60 m AGL, 80 m AGL, 100 m AGL). Then, we have validated the results obtained adopting commercial omni-directional antennas with those obtained exploiting a new antennas system (composed by four 2×2 MIMO antennas) connecting to the nearest BTS (NBTS strategy), as well as maintaining the connection to the current BTS (CBTS strategy). The obtained results are promising and lead the conclusion that the first prototypical version of our proposed SSAS offers signal quality gains and network stability improvements when the UAV flyes above a certain flight altitude (namely, above 60 m AGL). Finally, we have highlighted possible future research directions to improve and enhance the gain possibly obtainable through the adoption of our proposed SSAS on flying drones in BVLOS scenarios.

REFERENCES

[1] *Drone Strategy: Creating a Large-Scale European Drone Market*, Directorate-Gen. Mobility Transp., Transp. News, Nov. 2022. Accessed: Nov. 21, 2023. [Online]. Available: https://transport.ec.europa.eu/news-events/news/drone-strategycreating-large-scale-european-drone-market-2022-11-29_en

[2] Grand View Research, Inc. (2023). *Commercial Drone Market Size, Share & Trends Analysis Report*. Accessed: Nov. 21, 2023. [Online]. Available: https://www.grandviewresearch.com/industry-analysis/global-commercial-drones-market

[3] (2020). *DJI Official Website*. Accessed: Nov. 21, 2023. [Online]. Available: https://www.dji.com/

[4] (2019). *What is DJI OcuSync and How Does it Work?* Accessed: Nov. 21, 2023. [Online]. Available: https://store.dji.bg/en/blog/what-is-dji-ocusync-and-how-does-it-work

[5] Parrot. (2021). *ANAFI AI: The 4G Robotic UAV*. Accessed: Nov. 21, 2023. [Online]. Available: https://www.parrot.com/en/drones/anafi-ai

[6] *European Union Aviation Safety Agency (EASA)*. Accessed: Nov. 21, 2023. [Online]. Available: https://www.easa.europa.eu/

[7] *Evolved Universal Terrestrial Radio Access (E-UTRA); Physical Layer—Measurements*, document TS 36.214, 3GPP, European Telecommunications Standards Institute (ETSI), Apr. 2017. [Online]. Available: https://tinyurl.com/ETSITS136214

[8] D. C. Montgomery and G. C. Runger, *Applied Statistics and Probability for Engineers*. Hoboken, NJ, USA: Wiley, 2011.

[9] A. N. Kolmogorov, *Kolmogorov–Smirnov Test*. New York, NY, USA: Springer, 1939, pp. 283–287.

[10] P. Guckian, "LTE unmanned aircraft systems trial report," Qualcomm, Chennai, India, Trial Rep. 1.0.1, May 2017. [Online]. Available: https://www.qualcomm.com/content/dam/qcomm-martech/dm-assets/documents/lte-unmanned-aircraft-systems-trial-report.pdf

[11] M. A. Zulkifley, M. Behjati, R. Nordin, and M. S. Zakaria, "Mobile network performance and technical feasibility of LTE-powered unmanned aerial vehicle," *Sensors*, vol. 21, no. 8, p. 2848, Apr. 2021, doi: 10.3390/s21082848.

[12] A. Fotouhi, H. Qiang, M. Ding, M. Hassan, L. G. Giordano, A. Garcia-Rodriguez, and J. Yuan, "Survey on UAV cellular communications: Practical aspects, standardization advancements, regulation, and security challenges," *IEEE Commun. Surveys Tuts.*, vol. 21, no. 4, pp. 3417–3442, 4th Quart., 2019, doi: 10.1109/COMST.2019.2906228.

[13] X. Lin, R. Wiren, S. Euler, A. Sadam, H.-L. Määttänen, S. Muruganathan, S. Gao, Y.-P. E. Wang, J. Kauppi, Z. Zou, and V. Yajnanarayana, "Mobile network-connected drones: Field trials, simulations, and design insights," *IEEE Veh. Technol. Mag.*, vol. 14, no. 3, pp. 115–125, Sep. 2019, doi: 10.1109/MVT.2019.2917363.

[14] *Enhanced LTE Support for Aerial Vehicles*, document TR 36.777, 3GPP, Jan. 2018. Accessed: Nov. 21, 2023. [Online]. Available: https://www.3gpp.org/ftp//Specs/archive/36_series/36.777/

[15] S. D. Muruganathan, X. Lin, H.-L. Määttänen, J. Sedin, Z. Zou, W. A. Hapsari, and S. Yasukawa, "An overview of 3GPP release-15 study on enhanced LTE support for connected drones," *IEEE Commun. Standards Mag.*, vol. 5, no. 4, pp. 140–146, Dec. 2021, doi: 10.1109/MCOMSTD.0001.1900021.

[16] W. D. Ivancic, R. J. Kerczewski, R. W. Murawski, K. Matheou, and A. N. Downey, "Flying drones beyond visual line of sight using 4G LTE: Issues and concerns," in *Proc. Integr. Commun., Navigat. Surveill. Conf. (ICNS)*, Herndon, VA, USA, Apr. 2019, pp. 1–13, doi: 10.1109/ICNSURV.2019.8735246.

[17] H. C. Nguyen, R. Amorim, J. Wigard, I. Z. KováCs, T. B. Sørensen, and P. E. Mogensen, "How to ensure reliable connectivity for aerial vehicles over cellular networks," *IEEE Access*, vol. 6, pp. 12304–12317, Feb. 2018, doi: 10.1109/ACCESS.2018.2808998.

[18] J. Lyu and R. Zhang, "Network-connected UAV: 3-D system modeling and coverage performance analysis," *IEEE Internet Things J.*, vol. 6, no. 4, pp. 7048–7060, Aug. 2019, doi: 10.1109/JIOT.2019.2913887.

[19] A. Colpaert, E. Vinogradov, and S. Pollin, "Aerial coverage analysis of cellular systems at LTE and mmWave frequencies using 3D city models," *Sensors*, vol. 18, no. 12, p. 4311, Dec. 2018, doi: 10.3390/s18124311.

[20] S. Zhang and R. Zhang, "Radio map-based 3D path planning for cellular-connected UAV," *IEEE Trans. Wireless Commun.*, vol. 20, no. 3, pp. 1975–1989, Mar. 2021, doi: 10.1109/TWC.2020.3037916.

[21] M. M. H. Mahfuz and C.-W. Park, "Review of patch antennas used in drone applications," *IEEE Access*, vol. 11, pp. 58367–58388, 2023, doi: 10.1109/ACCESS.2023.3284040.

[22] H. Lee, Y.-B. Kim, and H. L. Lee, "Reconfigurable antenna for UAV-assisted wide coverage air-to-ground communications," *IEEE Access*, vol. 10, pp. 88034–88042, 2022, doi: 10.1109/ACCESS.2022.3199700.

[23] K.-S. Kim, J.-S. Yoo, J.-W. Kim, S. Kim, J.-W. Yu, and H. L. Lee, "All-around beam switched antenna with dual polarization for drone communications," *IEEE Trans. Antennas Propag.*, vol. 68, no. 6, pp. 4930–4934, Jun. 2020, doi: 10.1109/TAP.2019.2952006.

[24] Dassault Systèmes. *CST Studio Suite 2020 Help*. Accessed: Nov. 21, 2023. [Online]. Available: https://tinyurl.com/spmitrad

[25] Sierra Wireless. *EM9191 5G NR Sub-6 GHz Module*. Accessed: Nov. 21, 2023. [Online]. Available: https://www.sierrawireless.com/iot-modules/5g-modules/em9191/

[26] (2019). *Techship MU201 Adapter (M.2 Key B to USB3 Type A, Dual SIM)*. Accessed: Nov. 21, 2023. [Online]. Available: https://techship.com/products/techship-mu201-adapter-m-2-key-b-to-usb3-type-a-dual-sim/

[27] ArduPilot. *Pixhawk Cube Orange*. Accessed: Nov. 21, 2023. [Online]. Available: https://tinyurl.com/ardupilot

[28] MAVLink. *MAVLink Developer Guide*. Accessed: Nov. 21, 2023. [Online]. Available: https://mavlink.io

[29] GeoPy. *GeoPy: Python Geocoding Toolbox*. Accessed: Nov. 21, 2023. [Online]. Available: https://geopy.readthedocs.io/en/stable/

[30] Daniel Ellis Research. (2020). *Calculating the Bearing Between Two Geospatial Coordinates*. Accessed: Nov. 21, 2023. [Online]. Available: https://towardsdatascience.com/calculating-the-bearing-between-two-geospatial-coordinates-66203f57e4b4

[31] J. Sedin, S. Euler, and X. Lin. *Drones and Networks: Mobility Support*. Accessed: Nov. 21, 2023. [Online]. Available: https://www.ericsson.com/en/blog/2019/1/drones-and-networks-mobility-support

GIORDANO CICIONI (Graduate Student Member, IEEE) received the B.Sc. and M.Sc. (magna cum laude) degrees in electronic engineering from the University of Perugia, Perugia, Italy, in 2017 and 2020, respectively, where he is currently pursuing the Ph.D. degree in industrial and information engineering with the High-Frequency Electronics Laboratory. During the Ph.D. studies, he was a Visiting Researcher with Institute für Mikrowellentechnik, Universität Ulm, Germany. His current research interests include the design and deployment of radar sensors for river monitoring and vibrometry applications. He was a recipient of the Second Place at the 3 Minute Thesis Competition held at IMS 2023.

VALENTINA PALAZZI (Senior Member, IEEE) received the M.S. degree in electrical engineering and the Ph.D. degree in industrial and information engineering from the University of Perugia, Italy, in 2014 and 2018, respectively. In 2015, she was a Visiting Ph.D. Student with the Tyndall National Institute, Cork, Ireland. In 2016, she did a short-term scientific mission with Centre Tecnològic de Telecomunicacions de Catalunya, Barcelona, Spain, sponsored by the Cost Action IC1301 "WiPE." From December 2016 to April 2017, she was a Student Intern with the Agile Technologies for High Performance Electromagnetic Novel Applications Research Group, School of Electrical and Computer Engineering, Georgia Institute of Technology, Atlanta, GA, USA. Since 2019, she has been a Researcher with the High Frequency Electronics Laboratory, Department of Engineering, University of Perugia. She has coauthored more than 60 articles and holds three patents. Her current research interests include the design of RF components, wireless sensors, radar front ends, wireless power transfer technologies, additive manufacturing processes, and conformal electronics. She was a recipient of the First Place Award of the Student Design Competition on Wireless Energy Harvesting at the 2016 IEEE MTT-S "International Microwave Symposium" (IMS), the IEEE MTT-S Graduate Fellowship, in 2017, the 2017 MTT-S Prize–Italy Chapter Central and Southern Italy, the International Union of Radio Science (URSI) Young Scientist Best Paper Award conferred at the 2019 URSI Italian National Meeting, the Second Place at the 3 Minute Thesis Competition held at IMS 2021, and the GAAS Young Scientist Recognition (URSI Commission D) at GASS 2021. She is the 2023 Microwave Theory and Technology Society (MTT-S) AdCom Secretary. She is the Chair of the IEEE MTT-S Technical Committee-26 RFID, Wireless Sensor and IoT, and the Early Career Representative of the Commission D "Electronics and Photonics" of the URSI.

EMANUELE PAGLIARI received the Dr.Ing. degree in communication engineering from the Department of Information Engineering, University of Parma, Italy, in 2020. He is currently pursuing the Ph.D. degree with the Internet of Things (IoT) Laboratory, Department of Engineering and Architecture, University of Parma. His research interests include the IoT, wireless communication systems, UAVs, and heterogeneous networking.

PAOLO MEZZANOTTE (Member, IEEE) was born in Perugia, Italy, in 1965. He received the Ph.D. degree from the University of Perugia, Perugia, in 1997. Since 2007, he has been an Associate Professor with the University of Perugia, where he has been involved in teaching the classes "radio-frequencies engineering" and "systems and circuits for IoT." He was the Vice Head of the Department of Engineering, University of Perugia, from 2014 to 2019. These research activities are testified by over 170 publications in the most reputed specialized journals and at the main conferences of the microwave scientific community. His present H-index is 22 (source Scopus). His current research interests include the development of microwave circuits on bio-compatible substrates and the enabling technologies for the IoT. He served as the Chair for the IEEE Technical Committee MTT-24-RFID Technologies for the biennium, from 2018 to 2019. He is the Chair of the IEEE Topical Conference on Wireless Sensors and Sensor Networks and an Associate Editor of *Applied Computational Electromagnetics Society Journal* and IEEE JOURNAL OF MICROWAVES.

LUCA DAVOLI (Member, IEEE) received the Dr.Ing. degree in computer engineering and the Ph.D. degree in information technologies from the Department of Information Engineering, University of Parma, Italy, in 2013 and 2017, respectively. He is currently a non-tenured Assistant Professor with the Internet of Things (IoT) Laboratory, Department of Engineering and Architecture, University of Parma. He is also a Research Scientist with things2i Ltd., a spin-off of the University of Parma dedicated to the IoT and smart systems. His research interests include the IoT, pervasive computing, big stream, and software-defined networking.

FEDERICO ALIMENTI (Senior Member, IEEE) received the Laurea (magna cum laude) and Ph.D. degrees in electronic engineering from the University of Perugia, Italy, in 1993 and 1997, respectively. He was a Visiting Scientist with the Technical University of Munich, Germany. Since 2001, he has been with the Department of Engineering, University of Perugia, teaching the class of RFIC design. From 2011 to 2014, he was the Scientific Coordinator of the ENIAC ARTEMOS Project. In summer 2014, he was a Visiting Professor with EPFL, Switzerland. He has participated in the Summer School 2017, held at Infineon Austria AG, Villach, as a Keynote Lecturer. In 2018, he got the qualification as a Full Professor. He has authored a European patent and more than 200 papers in journals, conferences, and books. His H-index is 26 with more than 2500 citations (source Scopus); and 23 with more than 2000 citations (source Google Scholar). His research interests include microwave and RFIC design. In 1996, he was a recipient of the URSI Young Scientist Award. In 2013, he was a recipient of the IET Premium (Best Paper) Award and the TPC Chair of the IEEE Wireless Power Transfer Conference. He won the ''Mario Sannino'' Award for the best research in the field of microwave electronics.

LUCA ROSELLI (Fellow, IEEE) joined the University of Perugia, Perugia, Italy, in 1991. In 2000, he founded the spin-off WiS Srl. He is currently a qualified Full Professor with the University of Perugia, where he teaches applied electronics and coordinates the High Frequency Electronics Laboratory. He has authored over 280 papers (H-index = 23, i10 = 51, over 2200 citations scholar) and *Green RFID System* (Cambridge University Press, 2014). He was involved in electronic technologies for the Internet of Things for six years. His current research interests include HF electronic systems with special attention to RFID, new materials, and wireless power transfer. He was a member of the Board of Directors of ART Srl, Urbino, Italy, from 2008 to 2012. He is a member of the list of experts of the Italian Ministry of Research, the past Chair of the IEEE Technical Committees MTT-24-RFID, the Vice Chair of 25-RF Nanotechnologies, 26-Wireless Power Transfer, the ERC Panel PE7, the Advisory Committee of the IEEE-WPTC, and the Chairperson of the SC-32 of IMS. He is the Co-Chair of the IEEE Wireless Sensor Network Conference. He organized the VII Computational Electromagnetic Time Domain, in 2007, and the first IEEE Wireless Power Transfer Conference, in 2013. He is an Associate Editor of *IEEE Microwave Magazine*. He is involved on the boards of several international conferences. He is a Reviewer of many international reviews, including the PROCEEDINGS OF THE IEEE, IEEE TRANSACTIONS ON MICROWAVE THEORY AND TECHNIQUES, and IEEE MICROWAVE AND WIRELESS COMPONENTS LETTERS.

GIANLUIGI FERRARI (Senior Member, IEEE) received the Laurea (summa cum laude) and Ph.D. degrees in electrical engineering from the University of Parma, Parma, Italy, in 1998 and 2002, respectively. Since 2002, he has been with the University of Parma, where he is currently a Full Professor of telecommunications and also the Coordinator of the Internet of Things (IoT) Laboratory, Department of Engineering and Architecture. He is the Co-Founder and the President of things2i Ltd. (http://www.things2i.com/), a spin-off of the University of Parma dedicated to the IoT and smart systems. His current research interests include signal processing, advanced communication and networking, the IoT, and smart systems. More information can be found at: http://www.tlc.unipr.it/ferrari/.

• • •